Delft University of Technology

Exploring Millimeter-Wavelength Radar Capabilities for Raindrop Size Distribution Retrieval

Estimating Mass-Weighted Mean Diameter from the Differential Backscatter Phase

Unal, Christine; van den Brule, Yannick

DOI
10.1175/JTECH-D-23-0094.1

Publication date
2024

Document Version
Final published version

Published in
Journal of Atmospheric and Oceanic Technology

Citation (APA)
Unal, C., & van den Brule, Y. (2024). Exploring Millimeter-Wavelength Radar Capabilities for Raindrop Size Distribution Retrieval: Estimating Mass-Weighted Mean Diameter from the Differential Backscatter Phase. *Journal of Atmospheric and Oceanic Technology*, *41*(6), 583-603. https://doi.org/10.1175/JTECH-D-23-0094.1

Exploring Millimeter-Wavelength Radar Capabilities for Raindrop Size Distribution Retrieval: Estimating Mass-Weighted Mean Diameter from the Differential Backscatter Phase

CHRISTINE UNAL[a,b] AND YANNICK VAN DEN BRULE[a]

[a] Department of Geoscience and Remote Sensing, Delft University of Technology, Delft, Netherlands
[b] Climate Institute, Delft University of Technology, Delft, Netherlands

(Manuscript received 30 July 2023, in final form 29 March 2024, accepted 22 April 2024)

ABSTRACT: Accurate precipitation characterization relies on the estimation of raindrop size distribution (RDSD) from observations. While various techniques using centimeter-wavelength radars have been proposed for RDSD retrieval, the potential of millimeter-wavelength polarimetric radars, offering enhanced spatial and temporal resolution while capturing light to moderate rain, remains unexplored. This study focuses on retrieving the mass-weighted mean diameter D_m using a dual-frequency cloud radar. Since the differential reflectivity Z_{dr} is ineffective for D_m retrieval at 94 GHz, and simulations demonstrate a strong dependence of the differential backscatter phase δ_{co} on D_m, the estimation of δ_{co} takes precedence in this paper. Notably, δ_{co} remains unaffected by attenuation and polarimetric calibration. Addressing the initial requirement of disentangling backscattering and propagation effects at millimeter wavelength, an automatic algorithm is proposed to detect Rayleigh plateaus in the spectral domain. Subsequently, a methodology for estimating δ_{co} and its associated error is presented. Leveraging simulation results, confidence intervals for D_m that align with δ_{co} confidence intervals are retrieved. The assessment of D_m and its confidence interval at 35 and 94 GHz is conducted employing disdrometer-derived D_m. The results demonstrate a comprehensive concordance within a margin of 0.2 mm, underscoring the cloud radar's efficacy in delineating nuanced variations in the raindrop mean diameter versus altitude. The validation process encounters difficulties for D_m below 1 mm, as the disdrometer-derived D_m may exhibit an overestimation, while the cloud-radar-derived D_m may exhibit an underestimation. The combination of 35 and 94 GHz serves to diminish the confidence interval associated with the retrieved D_m.

KEYWORDS: Drop size distribution; Atmospheric profilers; Radars/Radar observations

1. Introduction

Compared to the rainfall rate, the raindrop size distribution (RDSD) provides a comprehensive description of rain microphysics (Jameson and Kostinski 2001). In situ sensors like disdrometers have been used to measure this distribution at ground level (Thurai et al. 2014; Gatidis et al. 2020). However, obtaining vertical profiles of RDSD is crucial for understanding microphysical processes such as evaporation, breaking, aggregation, and size sorting (Kumjian and Ryzhkov 2012). These profiles are essential for improving weather forecast parameterization, cloud-resolving models, and assessing changes in the precipitation type related to a warmer climate.

Various methodologies have been developed for obtaining vertical profiles of RDSD using centimeter-wavelength radar polarimetric measurements. For instance, Gatidis et al. (2022) assumed a normalized gamma model for the RDSD and utilized radar variables such as reflectivity factor and differential reflectivity, combined with a μ–λ relationship. Other techniques rely on measuring Doppler power spectra using vertically or slantwise profiling radar and exploiting the relationship between measured Doppler velocity and terminal fall velocity of raindrops (Williams 2002; Moisseev and Chandrasekar 2007; Unal 2015; Peters et al. 2005). However, due to a large radar beamwidth, for example, 2°, the retrieved raindrop size distributions primarily relate to medium-scale radar resolution volumes, limiting the observation of small-scale processes and comparison with in situ measurements.

In midlatitude regions, precipitation predominantly manifests as rainfall events typified by precipitation rates below 10 mm h^{-1}. Such conditions account for approximately 90% of the total rain volume observed across Europe (Mugnai et al. 2005). Overeem et al. (2023) more recently showed the prevalence of this primary rain regime through a comparative analysis of weather radar and gauge-derived 1-h precipitation depth spanning the period from 2013 to 2020. The nature of these rainfall events facilitates the utilization of millimeter-wavelength radar data for the retrieval of RDSD.

These cloud radars offer superior spatial, temporal, and Doppler velocity resolutions, particularly at 94 GHz (Kollias et al. 2002). However, the backscattered signal at millimeter wavelengths, especially 94 GHz, is significantly attenuated in the presence of liquid water, making these high-frequency radars suitable for studying light to moderate precipitation, where attenuation corrections are still possible. Kollias et al. (2007, 2020) provided an overview of millimeter-wavelength radar and their significance in the ARM radar network, respectively. Cloud radars are also deployed in Europe, with a focus on vertical profiling for cloud studies (Illingworth et al. 2007; Küchler et al. 2017). A new generation of cloud radars with polarimetric (Myagkov et al. 2020) and dual-frequency (35–94 GHz) capabilities has been developed.

Corresponding author: Christine Unal, c.m.h.unal@tudelft.nl

DOI: 10.1175/JTECH-D-23-0094.1

In the realm of cloud and precipitation remote sensing, the literature delves into retrieval methodologies tailored for cloud containing liquid and/or ice particles, as well as rain, predominantly employing vertical profiling measurements (Hogan et al. 2005; Bühl et al. 2015; Kneifel et al. 2015; Matrosov 2017; Mason et al. 2017; Tridon et al. 2017; among others). Matrosov (2017) proposed a method for retrieving the mass-weighted mean raindrop diameter, leveraging the disparity in mean Doppler velocities observed at Ka and W bands. Mason et al. (2017) formulated an algorithm tailored for multifrequency airborne radar data, incorporating W-band measurements into their approach. Meanwhile, Tridon and Battaglia. (2015) advanced a retrieval technique for raindrop size distribution, utilizing dual-frequency cloud radar Doppler spectra obtained through the vertical profiling mode. Subsequent refinement and application of this technique were documented in Tridon et al. (2017). However, a notable research gap persists in the domain of retrievals at millimeter wavelengths, specifically employing polarimetry and/or spectral polarimetry, necessitating the utilization of slant profiling or range–height indicator (RHI) measurement modes. This study directs its focus toward raindrop size distribution retrieval techniques at millimeter wavelengths, relying on polarimetric/spectral polarimetric data, similar to what has been done for weather radars operating at centimeter wavelengths. In these retrievals, the differential reflectivity Z_{dr} has been a key polarimetric measurement. However, at 94 GHz, Z_{dr} is not very sensitive to variations in the raindrop size distribution (Aydin and Lure 1991; Myagkov et al. 2020). Therefore, this paper focuses on studying the differential backscatter phase as a proxy for mass-weighted mean raindrop diameter, a parameter of the raindrop size distribution. At frequencies of 35 and 94 GHz, the Mie scattering of spheroids generally describes the scattering of raindrops. As a result, the differential backscatter phase is expected to be larger than 0°. However, the cloud radar's differential phase includes both the differential propagation phase and the differential backscatter phase, necessitating the separation of these components. Instead of using an optimal estimation method, which can be computationally intensive (Tridon et al. 2017), this study places emphasis on a single radar variable to examine its ability to retrieve the small-scale variability of one RDSD parameter.

The manuscript is organized into several sections. Section 2 presents the simulation work for radar polarimetric and spectral polarimetric variables at 35 and 94 GHz related to rain. Section 3 introduces the sensors utilized in the experimental part of the study, along with an overview of the data employed. To address the disentanglement of the differential phase, section 4 outlines an automatic algorithm designed for detecting Rayleigh plateaus. One of the outcomes of this algorithm is the estimation of the differential backscatter phase, including its associated error, as expounded in section 5. Section 6 introduces the second automated algorithm devised for the estimation of the mass-weighted mean diameter and employing the confidence interval of estimated δ_{co}. The subsequent section, section 7, presents an initial comparison between the obtained mass-weighted mean raindrop diameter estimation and disdrometer data. Finally, section 8 concludes the paper by summarizing the key findings.

2. Simulation

The simulation proposed in this study aims to explore the trends in radar rain measurements across different frequencies. The backward S and forward F scattering amplitudes of raindrops are numerically obtained using the Fredholm integral method (Holt et al. 1978; Otto and Russchenberg 2011). The complex refractive index model for water, based on Liebe et al. (1991), incorporates the single Debye model for weather and Micro Rain Radar frequencies, and the double Debye model for cloud radars. Temperature T is allowed to vary within the range of 1°–40°C, while the radar elevation angle can be selected from 0° to 90°. The raindrop size distribution denoted as $N(D)$ (mm^{-1} m^{-3}) follows a gamma distribution normalized with respect to the liquid water content:

$$N(D) = N_w f(\mu)\left(\frac{D}{D_m}\right)^{\mu} \exp\left[-(4+\mu)\frac{D}{D_m}\right] \quad \text{with}$$

$$f(\mu) = \frac{6}{4^4}\frac{(4+\mu)^{\mu+4}}{\Gamma(\mu+4)}, \tag{1}$$

where the intercept parameter N_w, the mass-weighted mean diameter D_m, and the shape parameter μ parameterize the raindrop size distribution.

The RDSD is truncated to equivolume spherical diameters D ranging from 0.1 to 8 mm, with a step size of 0.079 mm. In this section, raindrops are modeled as oblate spheroids, employing a combination of axis ratio models described by Keenan et al. (2001) for $D < 1.35$ mm, Andsager et al. (1999) for 1.35 mm $\le D \le$ 4.4 mm, and Beard and Chuang (1987) for $D > 4.4$ mm. This combined shape–size relationship is referred to as KAB. Nonetheless, other axis ratio models can be selected for examining the impact of the models on the radar variables. Furthermore, the axial distribution (Mardia 1972) describes the orientation angle to account for the small canting of raindrops (Bringi and Chandrasekar 2001, 68–69). Finally, the estimation of the rainfall rate is conducted using the terminal fall velocity model (Bringi and Chandrasekar 2001, p. 414).

a. Radar polarimetric variables

The simulation provides the polarimetric measurements, including differential reflectivity [Z_{dr} (dB), (2), Figs. 1a,b], specific differential attenuation [A_{dp} (dB km^{-1}), (3), Figs. 1c,d], differential backscatter phase [δ_{co} (°), (4), Figs. 2a,b], and specific differential phase [K_{dp} (° km^{-1}), (5), Figs. 2c,d]. These variables are plotted for various raindrop size distributions while maintaining a rainfall rate constraint of less than 20 mm h^{-1} for K_{dp} at 94 GHz. It should be noted that the W-band cloud radar is not designed for measuring heavy or extreme precipitation due to significant attenuation. For the 35-GHz radar, the rainfall rate constraint is set at 30 mm h^{-1}:

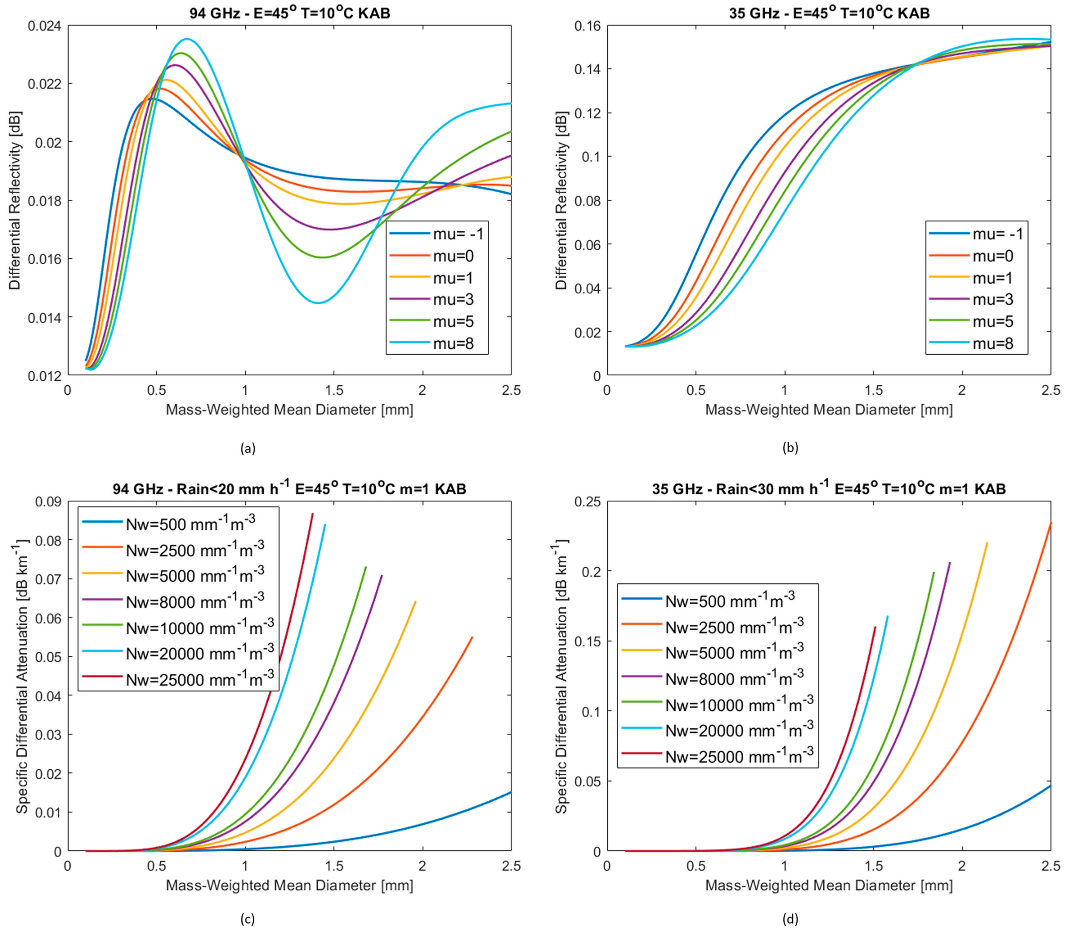

(a) (b)

(c) (d)

FIG. 1. Polarimetric cloud radar power variables versus gamma-modeled raindrop size distribution parameters in the case of the KAB axis ratio model. The elevation angle is 45°.

$$Z_{\mathrm{dr}}(\lambda, T, \alpha, D_m, \mu, r, \kappa) = 10\log_{10}\left[\frac{\displaystyle\int |S_{\mathrm{HH}}(\lambda,T,D)|^2 N(D)dD}{\displaystyle\int |S_{\mathrm{VV}}(\lambda,T,\alpha,D)|^2 N(D)dD}\right], \tag{2}$$

$$A_{\mathrm{dp}}(\lambda, T, \alpha, D_m, \mu, N_w, r, \kappa) = 8.686 \times 10^3 \frac{2\pi}{k_0}\Im\left\{\int [F_{\mathrm{HH}}(\lambda, T, D) - F_{\mathrm{VV}}(\lambda, T, \alpha, D)]N(D)dD\right\}, \tag{3}$$

$$\delta_{\mathrm{co}}(\lambda, T, \alpha, D_m, \mu, r, \kappa) = \frac{180^\circ}{\pi}\arg\left[\int S^*_{\mathrm{HH}}(\lambda, T, D) \times S_{\mathrm{VV}}(\lambda, T, \alpha, D)N(D)dD\right], \tag{4}$$

$$K_{\mathrm{dp}}(\lambda, T, \alpha, D_m, \mu, N_w, r, \kappa) = 10^3 \frac{180^\circ}{\pi}\frac{2\pi}{k_0}\Re e\left\{\int [F_{\mathrm{HH}}(\lambda, T, D) - F_{\mathrm{VV}}(\lambda, T, \alpha, D)]N(D)dD\right\}, \tag{5}$$

where λ and k_0 are the free space radar wavelength and wavenumber, respectively, α is the radar beam elevation angle, and r and κ relate to the axis ratio model and width of the orientation angle distribution, respectively. The S_{HH} and S_{VV} are the backscattering amplitudes, and F_{HH} and F_{VV} are the forward scattering amplitudes when horizontal or vertical polarization is used for transmission and reception, respectively.

Upon examining the small values of Z_{dr} in Fig. 1a, it becomes apparent that this variable is not suitable for retrieving the raindrop size distribution at 94 GHz. Similar small Z_{dr} values were previously observed in the simulations conducted by Aydin and Lure (1991). The Z_{dr} is independent of the number concentration. Another variable δ_{co}, also independent of the number concentration, can potentially replace Z_{dr} at 94 GHz, as suggested by Myagkov et al. (2020). Phase variables offer advantages over power measurements as they are not affected by attenuation at high frequencies.

Furthermore, it is worth noting that δ_{co} exhibits sensitivity to small mass-weighted mean diameter D_m values at 94 GHz, as depicted in Fig. 2a. However, this is not the case for K_{dp} shown in Fig. 2c. For D_m values below 0.5 mm, K_{dp} remains close to 0° km^{-1}. It should be emphasized that the differential

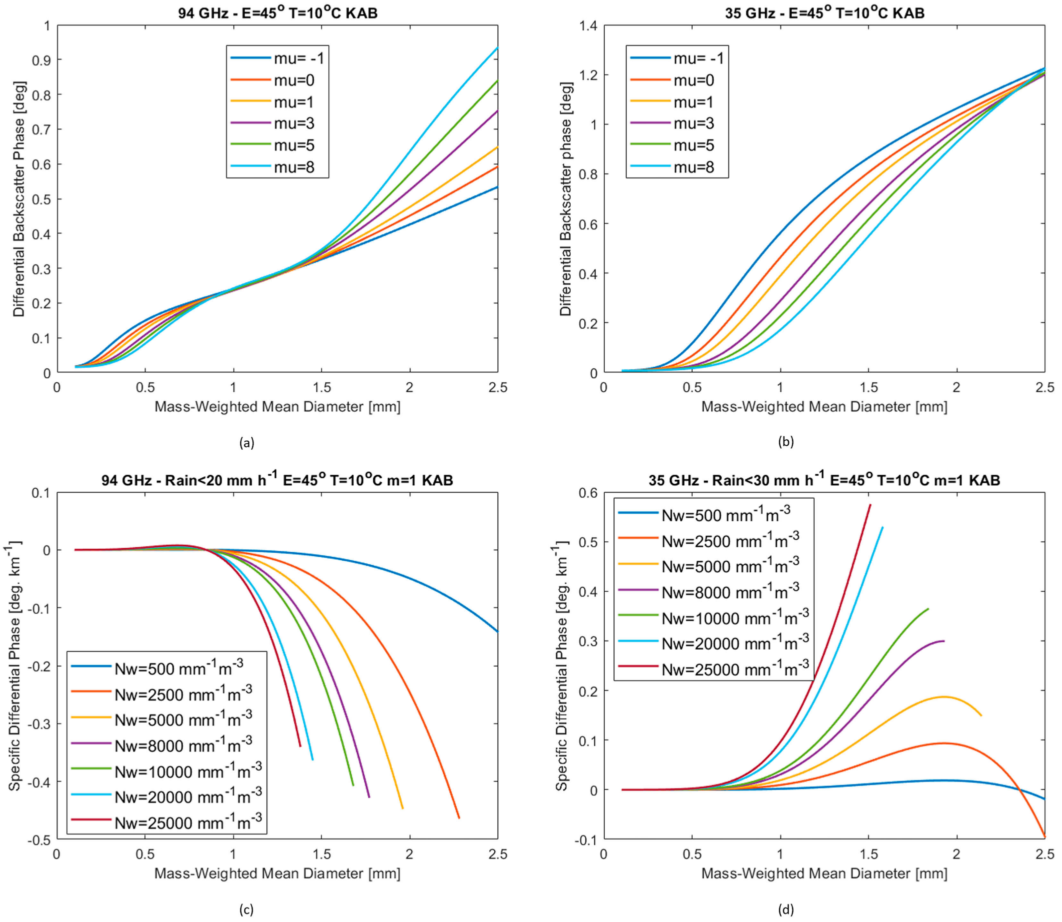

FIG. 2. Polarimetric cloud radar phase variables versus gamma-modeled raindrop size distribution parameters in the case of the KAB axis ratio model. The elevation is 45°.

propagation phase at 94 GHz decreases with range, while generally increasing at 35 GHz. Nonetheless, in instances of high rainfall rate and D_m, K_{dp} may become negative at 35 GHz.

In general, with the exception of the differential backscatter phase, the polarimetric variables at elevation 45° exhibit relatively diminutive values, presenting challenges in terms of both measurement and processing. In Figs. 1 and 2, a canting angle distribution with a standard deviation of 7° ($\kappa = 30$) is selected, which influences the range of polarimetric radar variables. The absence of the canting angle distribution results in an approximately twofold increase in their range.

To ensure equitable comparison of the propagation variables A_{dp} and K_{dp} at 94 and 35 GHz, a consistent rainfall rate threshold of 20 mm h^{-1} is applied. This standardization leads to a narrowed value range at 35 GHz, specifically (0, 0.15) dB km^{-1} and $(-0.05, 0.35)°$ km^{-1} for A_{dp} and K_{dp}, respectively. Consequently, in rainy conditions, K_{dp} is anticipated to be greater and A_{dp} smaller at 94 GHz compared to 35 GHz.

b. Doppler polarimetric spectra

In addition, the simulation provides Doppler polarimetric spectra like the spectral reflectivity (dBZ),

$$sZ_{\mathrm{HH}}(\lambda, T, D, D_m, \mu, N_w) = 10\log_{10}\left\{\frac{\lambda^4}{\pi^5|K_w(\lambda,T)|^2}N(D) \times [4\pi|S_{\mathrm{HH}}(\lambda,T,D)|^2]dD\right\}, \quad (6)$$

the spectral differential reflectivity (dB),

$$sZ_{\mathrm{dr}}(\lambda, T, \alpha, D, r, \kappa) = 10\log_{10}\left[\frac{|S_{\mathrm{HH}}(\lambda,T,D)|^2}{|S_{\mathrm{VV}}(\lambda,T,\alpha,D)|^2}\right], \quad (7)$$

and the spectral differential backscatter phase (°),

$$s\delta_{\mathrm{co}}(\lambda, T, \alpha, D, r, \kappa) = \frac{180°}{\pi}\arg[S^*_{\mathrm{HH}}(\lambda, T, D)S_{\mathrm{VV}}(\lambda, T, \alpha, D)]. \quad (8)$$

Note that the spectral differential reflectivity and spectral differential backscatter phase are independent of the raindrop size distribution, which prevents the retrieval of the raindrop size distribution. Nonetheless, in instances of drizzle or very light rain, the absence of Mie oscillations in sZ_{dr} and $s\delta_{\mathrm{co}}$ becomes apparent when medium to large raindrops are absent.

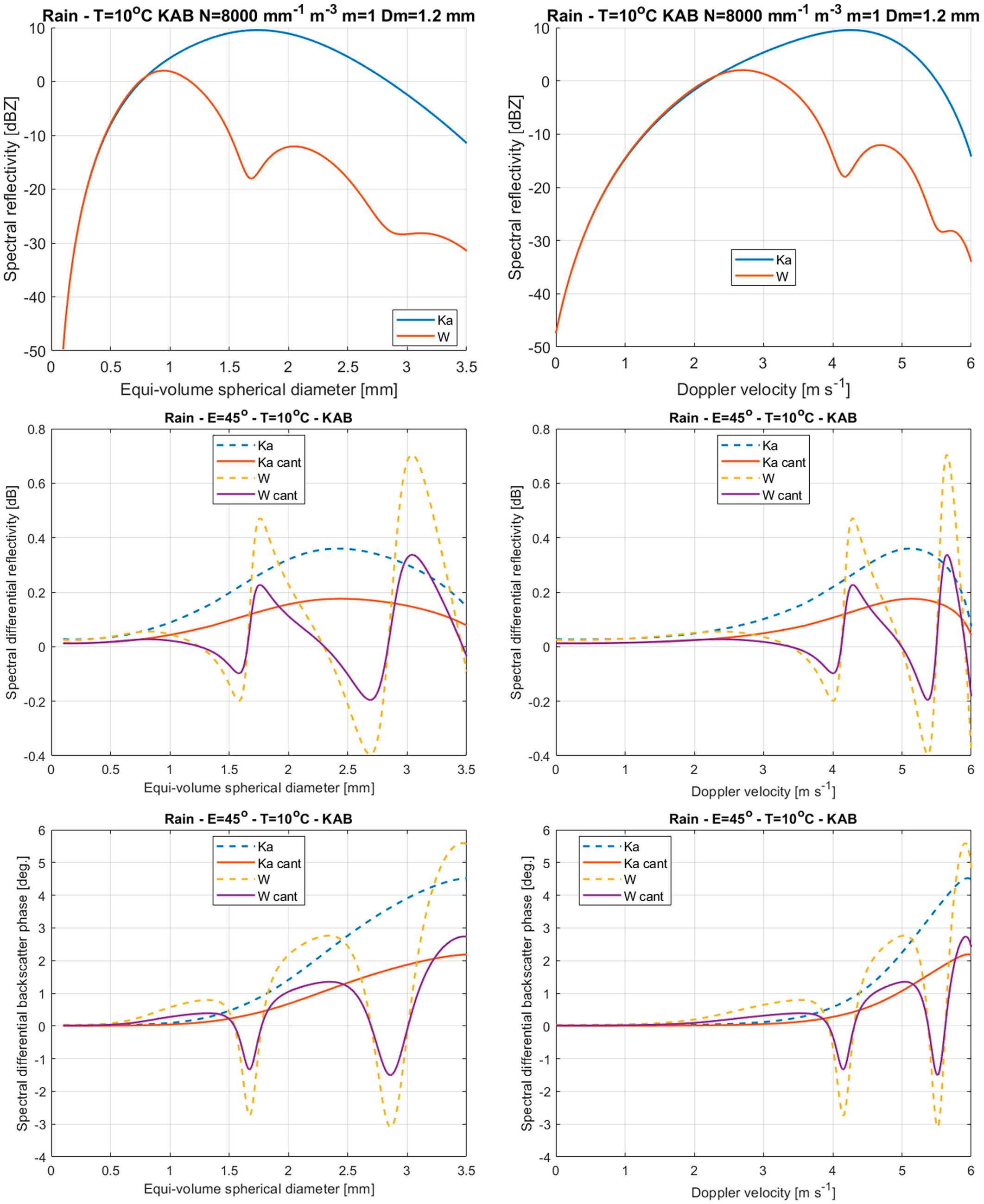

FIG. 3. Doppler polarimetric radar variables sZ_{HH}, sZ_{dr}, and $s\delta_{\mathrm{co}}$ versus the (left) equivolume spherical diameter and (right) Doppler velocity. No canting angle distribution is applied for the dashed lines.

For illustration purposes, we set the temperature at $T = 10°\mathrm{C}$ and employ the raindrop size distribution parameters ($D_m = 1.2$ mm, $\mu = 1$, and $N_w = 8000\ \mathrm{mm}^{-1}\ \mathrm{m}^{-3}$) to achieve a corresponding rainfall rate of 3.2 mm h^{-1}. In the top panel of Fig. 3, we present the Doppler power spectra within the cloud radar frequency bands. Note that the plotted spectral reflectivity adheres to (6), implying its integration over diameter or Doppler velocity resolution. Additionally, in Fig. 3, we portray sZ_{dr} (middle) and $s\delta_{\mathrm{co}}$ (bottom) as functions of equivolume spherical diameter and Doppler velocity [(9)], maintaining a fixed radar elevation angle of 45°, temperature, and the shape–size relationship (KAB). The peak values of both sZ_{dr} and $s\delta_{\mathrm{co}}$ decrease with an increase in the wobbling of raindrops.

The influence of the Mie scattering regime, characterized by oscillatory behavior, is clearly observed for all variables at the cloud radar frequencies (35 and 94 GHz). As the spectral reflectivity at 94 GHz increases versus D before reaching its first maximum at $D < 1$ mm, the Rayleigh scattering regime occurs for $D < 0.7$ mm. Within this regime, a Rayleigh plateau for $s\delta_{co}$ and sZ_{dr} can be identified, indicating that the raindrops are expected to be small compared to the radar wavelength and approximately spherical in shape. Consequently, sZ_{dr} tends to approach values near 0 dB (indicative of quasi-spherical shape), while $s\delta_{co}$ tends to approach 0° (representative of Rayleigh scattering). For the given example, at $D = 0.7$ mm, with an elevation angle of 45° and including raindrop canting, sZ_{dr} reaches 0.025 dB at both frequency bands, while $s\delta_{co}$ reaches 0.02° at 35 GHz and 0.1° at 94 GHz, respectively.

Using (9) (Atlas et al. 1973; Unal 2015),

$$v(D) = [9.65 - 10.3\exp(-0.6D)]\sin(\alpha), \tag{9}$$

the Doppler fall velocity yields a value of 2.04 m s^{-1} for $D = 0.7$ mm. Therefore, the width of the Rayleigh or Doppler spectral plateau is expected to be approximately 2.0 m s^{-1}.

In the examination of backscattering polarimetric variables, namely, Z_{dr} and δ_{co}, at both 94 and 35 GHz, as depicted in Figs. 1 and 2, it is observed that the range of their values is more restricted at 94 GHz when compared to 35 GHz. This disparity can be attributed to the occurrence of Mie oscillations for smaller raindrop diameters at 94 GHz as opposed to 35 GHz. When integrating over diameters to derive bulk variables, and considering the presence of Mie oscillations, a consequential reduction in the values of the bulk variables is anticipated.

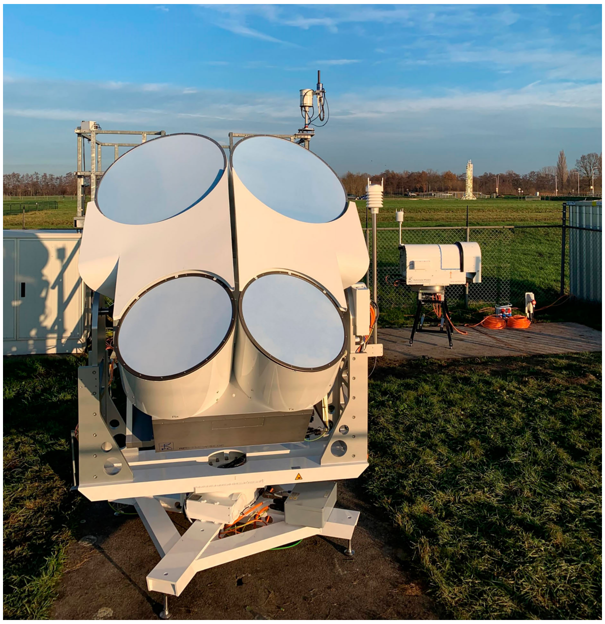

FIG. 4. Dual-frequency polarimetric scanning cloud radar (RPG-FMCW-DP-KW type), CLARA, after preliminary installation on the Cabauw site. The study case data were acquired in this configuration. Tiling and leveling the ground has been done afterward, including a 1-m platform for the radar. The radar is a frequency modulated continuous wave (FMCW) system with two antennas for transmission and reception at 35 and 94 GHz, top and bottom, respectively. On the right side, a pole carries the Vaisala meteorological weather station.

3. Sensors and data

For this study, a remote sensing instrument called Cloud Atmospheric Radar (CLARA) is used, which is a dual-frequency polarimetric radar operating at 35 and 94 GHz (Fig. 4). Additionally, an in situ sensor, Parsivel disdrometer, is employed. Both sensors are located at the national Ruisdael Observatory site in Cabauw, the Netherlands. The dual-frequency measurements are matched in terms of looking direction, sampling time, and range resolution. However, they differ in beamwidth, with values of 0.84° and 0.56° for 35 and 94 GHz, respectively, as well as the unambiguous maximum Doppler velocity. Table 1 presents the relevant radar specifications for the case study. The cloud radar beams are oriented in the west direction with an elevation angle of 45°, while the disdrometer is positioned 150 m away from the radar in the east direction. Moreover, a weather station is installed on the cloud radar frame to provide the rainfall rate.

Regarding calibration procedures, the monitoring of transmit power is conducted, and the radar receiver, inclusive of the receiving antenna, undergoes calibration every 6 months through a clear sky calibration method, utilizing microwave radiometer measurements. Additionally, short-term calibration is achieved through periodic Dicke switching. The receiver calibration yields gain factors associated with the intermediate frequency (IF) or range. In the context of utilizing polarimetric measurements for research, such as in this study, polarimetric calibration data are employed, leading to the correction of polarimetric variables at each range. Calibration data are gathered during vertical profiling or considering measurements of drizzle or very light rain at elevation angles other than 90°. In both scenarios, it is expected that Z_{dr} and Ψ_{dp} in rain will exhibit an average of 0 dB and 0°, respectively.

The case studies comprise 1 h of convective rain (no apparent melting layer) depicted in Figs. 5 and 6 and a time series of 5 h of stratiform precipitation shown in Fig. 7. Figures 5 and 6 focus on spectrograms corresponding to a rainfall rate of 15 mm h^{-1} at the ground level. The Doppler velocity, as observed, has a negative sign when raindrops exhibit motion toward the cloud radar. Contributions to this observed Doppler velocity stem from the combined effects of raindrop fall velocities and both horizontal and vertical wind components. Doppler aliasing occurs at 94 GHz. The Mie scattering regime is observed on the left side of the rain Doppler spectra. Specifically, the spectral differential phase $s\Psi_{dp}$ comprises a nearly constant phase relative to Doppler velocity (spectral differential propagation phase $s\Phi_{dp}$) and the spectral differential backscatter phase $s\delta_{co}$, which is nonzero in the Mie scattering regime and contingent on the Doppler velocity. The $s\Phi_{dp}$ exhibits either an increase or a decrease with height, for 35 and 94 GHz, respectively. At that stage, the system differential phase, which is quite small, −0.8° and −0.2° at 35 and 94 GHz, respectively, still contributes to the differential phase values.

TABLE 1. Dual-frequency cloud radar (CLARA) specifications for the rain case study (3 Feb 2021). (a) Common specifications at 35 and 94 GHz and (b) frequency dependent specifications.

(a) Common specifications		
Type	FMCW	
Polarimetry	STSR mode	
Time resolution	3.6 s	
Chirp 1 effective integration time	1.2 s	
Chirp 1 (rain)—Height		
Lowest height	84.3 m	
Maximum height	843.4 m	
Height resolution	21.1 m	
Beams		
Elevation	45°	
Azimuth	247°	
(b) Frequency dependent specifications		
Central frequency	35 GHz	94 GHz
Transmitted power	10.6 W	1.1 W
Chirp 1 (rain)—Doppler		
Max unambiguous velocity	19.7 m s^{-1}	7.3 m s^{-1}
Doppler resolution	15.5 cm s^{-1}	5.8 cm s^{-1}
Antennas		
Type	Bistatic Cassegrain 70-cm aperture	Bistatic Cassegrain 50-cm aperture
Separation	76.8 cm	56.8 cm
Beamwidth	0.84°	0.55°
Gain	47.6 dB	50.3 dB

Figure 7 illustrates a typical stratiform rain event during the winter period, primarily initiated by the ice phase, as is the case for most midlatitude precipitation events. The height of the melting layer varies between 1500 and 1000 m. The reflectivity data, which are direct radar outputs, are presented without attenuation correction and artifact filtering at this stage. Attenuation due to the liquid phase has a more significant impact at 94 GHz compared to 35 GHz, thereby reducing the sensitivity of the 94 GHz radar in the precipitating cloud region. To provide a comprehensive view, the rainfall rate data from the weather station are plotted in Fig. 8. At the ground level, the rainfall rate ranges from 0 to 7.5 mm h^{-1}, exhibiting significant variability within this 5-h time period. Figure 9 displays the corresponding Parsivel disdrometer binned raindrop size distributions. It is important to note that the Parsivel disdrometer is unable to measure raindrop sizes smaller than 0.25 mm. However, the RDSD distributions reveal that many small raindrops are missed in the first bin ($0.25 < D < 0.375$ mm), which may affect the estimation of the mass-weighed mean diameter (leading to overestimation), particularly for narrow distributions associated with light rain.

4. Automatic Rayleigh plateau detection

Both the specific differential phase K_{dp} and the differential backscatter phase δ_{co} hold potential for retrieving raindrop size distributions. The δ_{co} may provide an estimate of the mass-weighted mean diameter and K_{dp} relates to the raindrop number concentration. However, these variables are not directly measured by the cloud radar. Instead, the cloud radar provides measurements of the differential phase Ψ_{dp}, which is the sum of the differential propagation phase Φ_{dp} and the differential backscatter phase. This relationship is given by (10):

$$\Psi_{\mathrm{dp}}(r) = \Phi_{\mathrm{dp}}(r) + \delta_{\mathrm{co}}(r), \qquad (10)$$

where r represents the range in kilometers.

To separate the effects of propagation and scattering (Myagkov et al. 2020), in this work, the spectral differential reflectivity sZ_{dr} and spectral differential phase $s\Psi_{\mathrm{dp}}$ measurements will be utilized. The Rayleigh plateau, which characterizes small raindrops, can be described in terms of differential phase by (11), where v denotes the measured Doppler velocity:

$$s\Psi_{\mathrm{dp}}(r, v) = s\Phi_{\mathrm{dp}}(r, v) = \Phi_{\mathrm{dp}}(r). \qquad (11)$$

Henceforth, through the identification of the spectral segment corresponding to the Rayleigh regime, a mean value for $s\Psi_{\mathrm{dp}}$ can be computed and linked to the differential propagation phase. Subsequently, by subtracting Φ_{dp} from the overall Ψ_{dp}, calculated across the entire spectrum, the differential backscattering phase can be derived.

Consequently, the primary goal is to pinpoint a Doppler velocity range, recognized as the Rayleigh plateau, exclusively associated with small raindrops. Simulation results indicate that this range is expected to be [0, 2] m s^{-1}. However, it is advisable to implement a straightforward detection algorithm for the Rayleigh plateau due to the possibility of Doppler aliasing, variations in the elevation angle (leading to contribution of

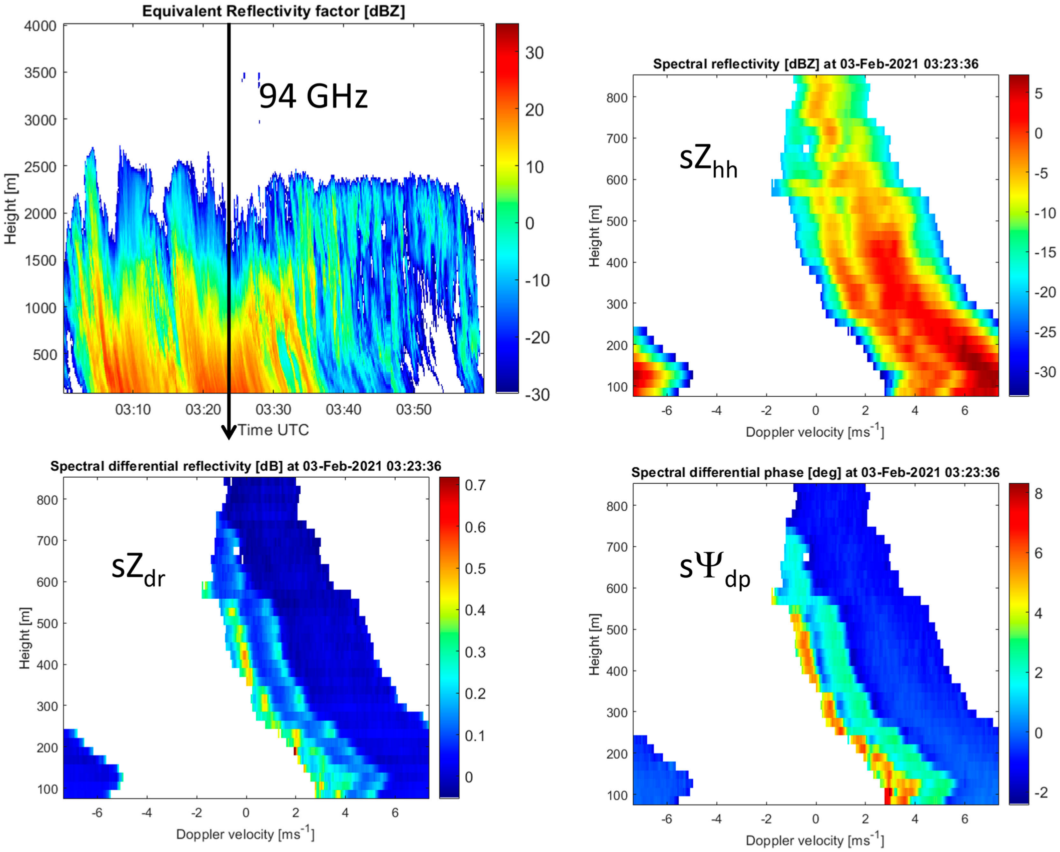

FIG. 5. Profiles of precipitation at 94 GHz with an example of spectrograms in rain up to 843 m.

the horizontal wind and change in the measured Doppler fall velocity width), and the dependency of Doppler velocity on height resulting from a decrease in air density.

a. *Algorithm*

The proposed algorithm, which must work for aliased Doppler spectra, comprises four steps and is implemented on spectra associated with rainfall rates exceeding 0.1 mm h^{-1}. Figure 10 provides a visualization of the algorithm. Steps 1–3 are applied to a fixed-height and time bin Doppler spectrum. Segments of the spectrum that do not align with the expected properties of the Rayleigh plateau are filtered out. Step 2 yields a collection of potential plateaus. In step 3, a cost function is established to determine the final selection of the Rayleigh plateau. Finally, step 4 repeats steps 1–3 for other height and time bins.

1) STEP 1 (DATA FILTERING)

The algorithm incorporates the spectral differential reflectivity and spectral differential phase in linear values. We use lowercase z and uppercase Z to represent the linear and dB values of the reflectivity, respectively. Only spectral data with a spectral signal-to-noise ratio (sSNR) greater than 15 dB are retained to reduce the variance of the spectral polarimetric variables at the edge of the spectra (Yu et al. 2012). At the Rayleigh plateau, a spectral differential reflectivity value of approximately 1 (0 dB) is anticipated due to the near-spherical shape of small raindrops. Consequently, values above 1.1 (0.41 dB) and below 0.9 (−0.46 dB) are eliminated through filtering. This filtering approach sufficed for our dataset, assuming accurate polarimetric calibration and moderate rain. For a distance of 1 km, the maximum two-way differential attenuation is 0.18 and 0.3 dB at 94 and 35 GHz, respectively, accounting for rainfall rates up to 20 mm h^{-1}. However, the lower threshold of 0.9 may be decreased at 35 GHz as the rainfall rate increases. Following these two straightforward filtering procedures, one based on spectral signal-to-noise ratio and the other one on sz_{dr}, the moving standard deviation of the spectral differential reflectivity sz_{dr}, denoted as std(sz_{dr}), is computed using five Doppler bins. This third filtering procedure involves excluding Doppler bins with std(sz_{dr}) $> 6 \times 10^{-3}$. This final threshold is chosen empirically. The outcome of this step is a vector containing the moving standard deviations of sz_{dr} and not-a-number (NaN) values. The corresponding Doppler velocities are known.

2) STEP 2 (REDUCTION OF POSSIBLE RAYLEIGH PLATEAUS)

In the context of this approach, the Rayleigh plateau may comprise any adjacent series of non-NaN values within the vector obtained from step 1. Assuming that the standard

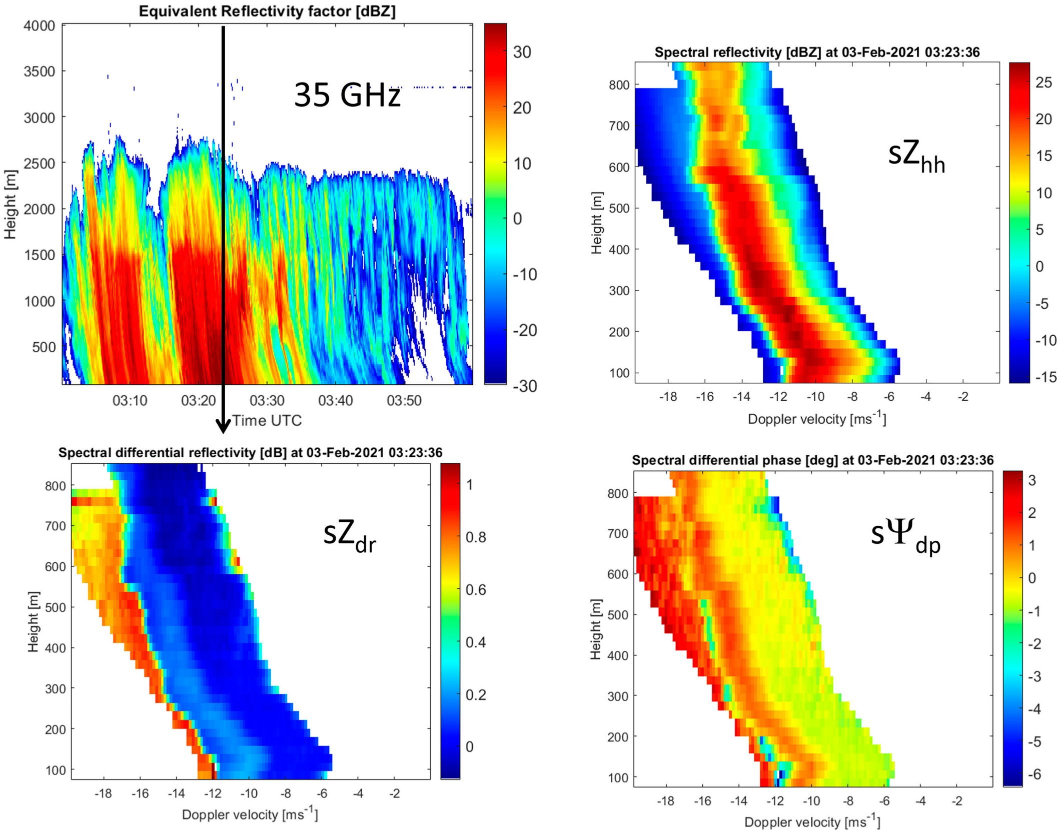
Equivalent Reflectivity factor [dBZ]

Spectral reflectivity [dBZ] at 03-Feb-2021 03:23:36

Spectral differential reflectivity [dB] at 03-Feb-2021 03:23:36

Spectral differential phase [deg] at 03-Feb-2021 03:23:36

FIG. 6. Profiles of precipitation at 35 GHz with an example of spectrograms in rain up to 843 m.

deviation vector contains 35 adjacent non-NaN values, there are a total of 595 possible series with a minimum length of 2, calculated as 35 × (35 − 1)/2. For each of these possibilities, a cost function is computed, leading to the identification of a single Rayleigh plateau at a specific height and time bin. To reduce the number of possibilities, series with a Rayleigh plateau length smaller than 10 values are filtered out. This criterion corresponds to a Doppler velocity spectrum width of 1.54 m s^{-1} for the 35-GHz band and 0.57 m s^{-1} for the 94-GHz band.

3) STEP 3 (RAYLEIGH PLATEAU SELECTION)

The cost function (CF) used to select the Rayleigh plateau from the possibilities generated in step 2 is defined as follows:

$$\mathrm{CF} = \frac{l}{l_{\max}} - 0.5\frac{sz_{\mathrm{dr,std}}}{sz_{\mathrm{dr,std,max}}} - 0.5\frac{s\Phi_{\mathrm{dp,std}}}{s\Phi_{\mathrm{dp,std,max}}}. \tag{12}$$

Here, l represents the length of the investigated plateau and $l_{\max}$ is the maximum length observed at the specific height

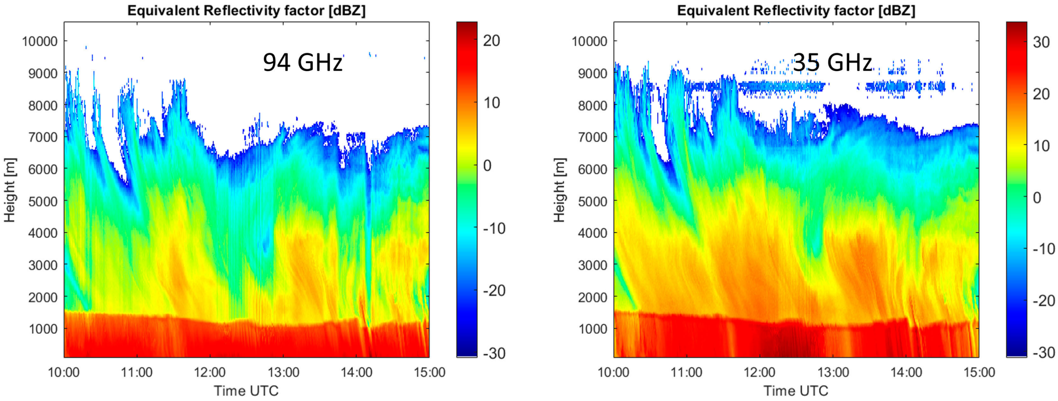
Equivalent Reflectivity factor [dBZ]

Equivalent Reflectivity factor [dBZ]

FIG. 7. Profiles of precipitation at (left) 94 and (right) 35 GHz on 3 Feb 2021.

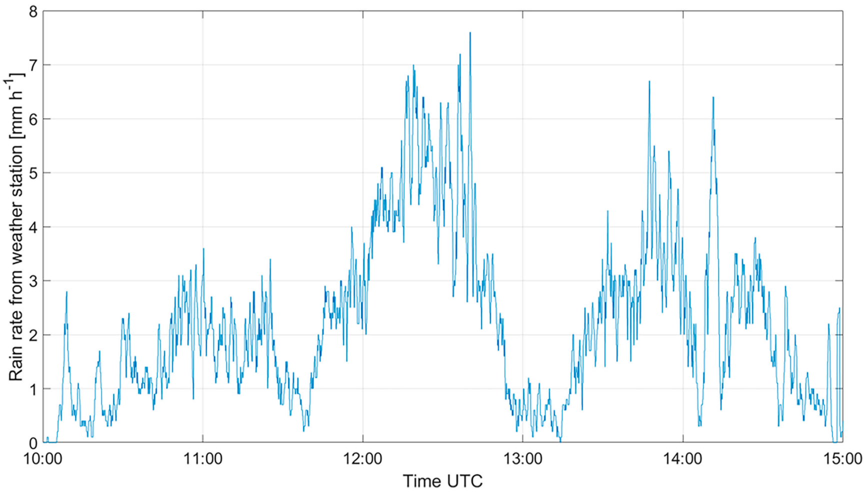

FIG. 8. Rainfall rate of the weather station at the cloud radar location on 3 Feb 2021.

and time bin. Both values are expressed in meters per second. A higher CF value indicates a more favorable candidate for the Rayleigh plateau. The preference is given to a broader plateau as it enables a more reliable average of the spectral differential reflectivity and spectral differential propagation phase. Consequently, the first term in (12) has a positive sign. The $sz_{\mathrm{dr,std}}$ denotes the standard deviation of all the spectral differential reflectivity values within the Rayleigh plateau possibility, while $sz_{\mathrm{dr,std,max}}$ represents the highest $sz_{\mathrm{dr,std}}$ value among all the possibilities. A lower standard deviation indicates a more favorable candidate since the Rayleigh plateau sz_{dr} remains relatively constant. Therefore, the second term in the equation has a negative sign. The same rationale applies to $s\Phi_{\mathrm{dp,std}}$, which represents the standard deviation of the spectral differential propagation phase. The Rayleigh plateau with the highest CF value is selected as the output of step 3.

The motivation behind executing steps 2–3 lies in securing a dependable Rayleigh plateau interval with sufficient data while mitigating the impact of edge values (characterized by noisy data for diminutive raindrops and the onset of the Mie scattering regime for the largest ones). These edge values possess the potential to exert influence on the averaged plateau value of Φ_{dp}.

4) STEP 4

Steps 1–3 are performed for every time and height bin at both 35- and 94-GHz frequencies. Consequently, approximately

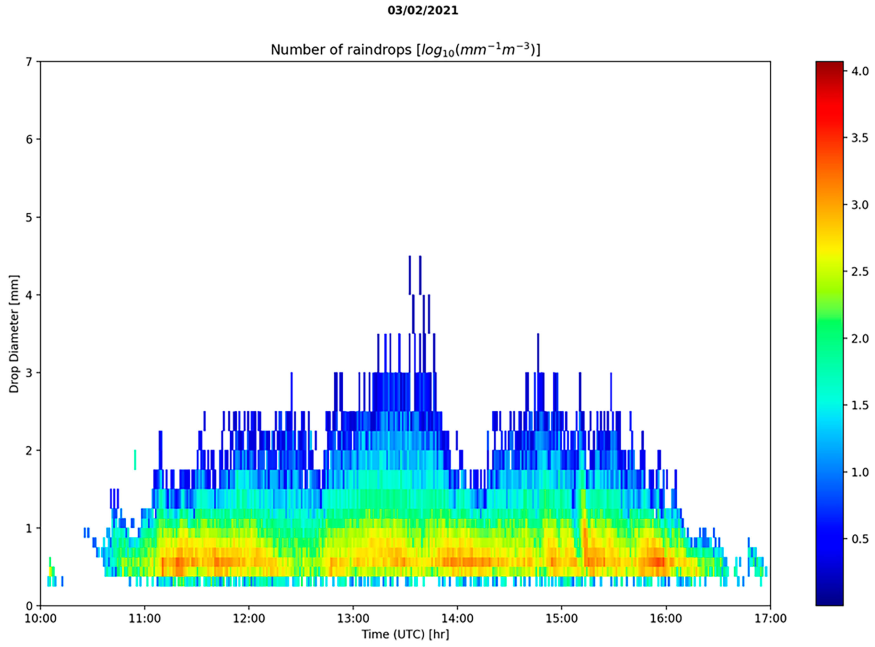

FIG. 9. Parsivel disdrometer data.

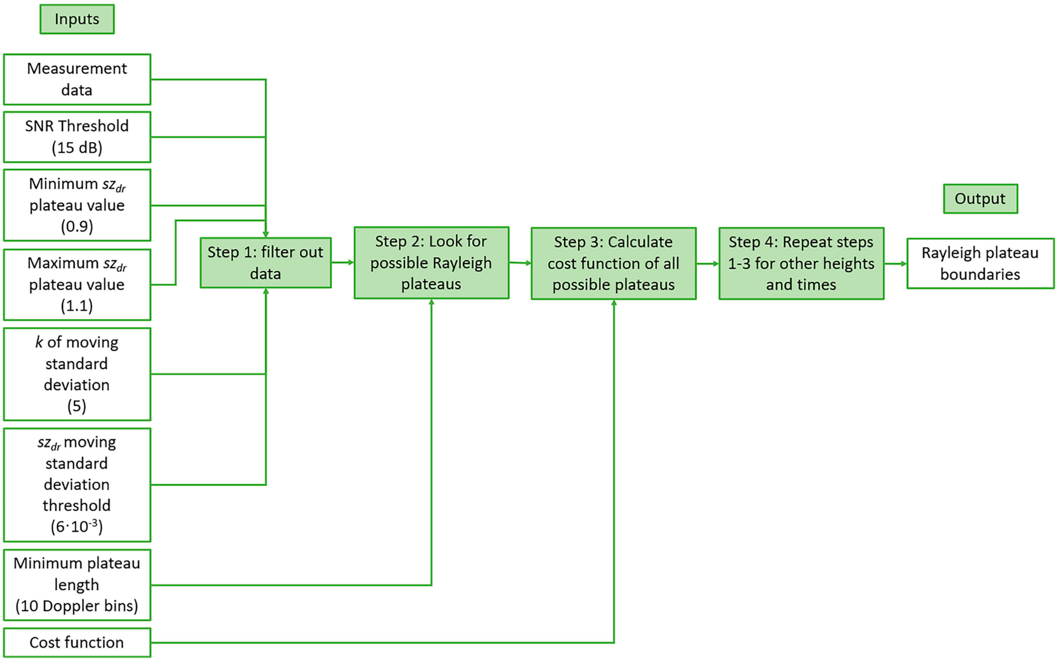

FIG. 10. Diagram showing the inputs, the four steps, and the output of the automated Rayleigh plateau detection algorithm.

69 510 Rayleigh plateaus are obtained per hour of rain measurement, corresponding to the product of 993 time bins, 35 height bins (during the winter season), and two frequency bands.

b. Illustration

Figure 11 illustrates an example of Rayleigh plateau detection for both 94- and 35-GHz frequency bands. At this stage, the absolute Doppler velocity lacks significance due to possible spectral aliasing and the presence of the radial horizontal wind component. The sSNR clipping at 15 dB restricts the visibility of only those parts of the spectra that significantly exceed the noise level. Generally, the 94-GHz Rayleigh plateau contains approximately three times more data compared to the 35-GHz plateau due to the higher Doppler resolution at 94 GHz. This greater quantity of data facilitates better detection of the Rayleigh plateau.

For the same rainfall rate at ground level (15 mm h^{-1}), Table 2 presents the Rayleigh plateau Doppler width, $sz_{\rm dr}$, and $s\Phi_{\rm dp}$, the latter serving as an estimate of $\Phi_{\rm dp}$ at the given height. As the height increases, the spectral differential reflectivity exhibits a slight decrease due to specific differential attenuation. For about 700 m, the differential attenuation is 0.026 and 0.014 dB at 35 and 94 GHz, respectively. Furthermore, at 94 GHz, the spectral differential propagation phase decreases with height ($K_{\rm dp}$ negative), while at 35 GHz, it increases with height ($K_{\rm dp}$ positive).

5. Estimation of the differential backscatter phase

a. Profiles at different rainfall rates

The differential phase $\Psi_{\rm dp}$ is calculated using the following equation:

$$\begin{aligned}\Psi_{\rm dp}(r) &= \frac{180^\circ}{\pi}\arg\left[\sum_{-v_{\rm max}}^{v_{\rm max}} C_{\rm HV}(r, v)\right]\\ &= \frac{180^\circ}{\pi}\arg\left[\int S^*_{\rm HH}(r, v)S_{\rm VV}(r, v)N(v)dv\right],\end{aligned} \tag{13}$$

where $C_{\rm HV}$ represents the measured cross-spectrum at sSNR = 15 dB. The estimation of the differential propagation phase involves averaging the spectral differential phase values obtained from the Rayleigh plateau. The resulting $\Phi_{\rm dp}$ is then subtracted from the calculated $\Psi_{\rm dp}$ to estimate $\delta_{\rm co}$ using (10). This subtraction ensures that the polarimetric calibration contained in $\Phi_{\rm dp}$ and $\Psi_{\rm dp}$ does not directly affect the values of the differential backscatter phase, providing a clear advantage.

Figure 12 illustrates an example of differential phase profiles resulting from the detection of the Rayleigh plateau. In Fig. 12a, with a rainfall rate of 15 mm h^{-1} at ground level, $\Phi_{\rm dp}$ decreases linearly with height from $-0.1°$ to $-1°$ over a range of 600 m, as $K_{\rm dp}$ is negative at 94 GHz. On the other hand, in Fig. 12b, at 35 GHz where $K_{\rm dp}$ is positive, $\Phi_{\rm dp}$ increases linearly from $-0.8°$ to $-0.3°$. These profiles correspond to $K_{\rm dp}$ values of $-1.5°$ and 0.83° km^{-1} for 94 and 35 GHz, respectively. The retrieved value of $\delta_{\rm co}$ remains relatively stable, averaging 0.5° and 1° for 94 and 35 GHz, respectively. These retrievals indicate a consistent raindrop size distribution between heights of 100 and 600 m.

From 600 to 800 m, a change in the raindrop size distribution (smaller D_m) is observed, indicated by the plateauing of $\Phi_{\rm dp}$ at $-1°$ and $-0.4°$, while $\delta_{\rm co}$ suddenly decreases to an average of 0.1° and 0.3° for 94 and 35 GHz, respectively. Figures 12c and 12d depict a case with a rainfall rate of 1 mm h^{-1}, where $\Phi_{\rm dp}$ and $\Psi_{\rm dp}$ coincide, and $\delta_{\rm co}$ is approximately 0°. In such a case,

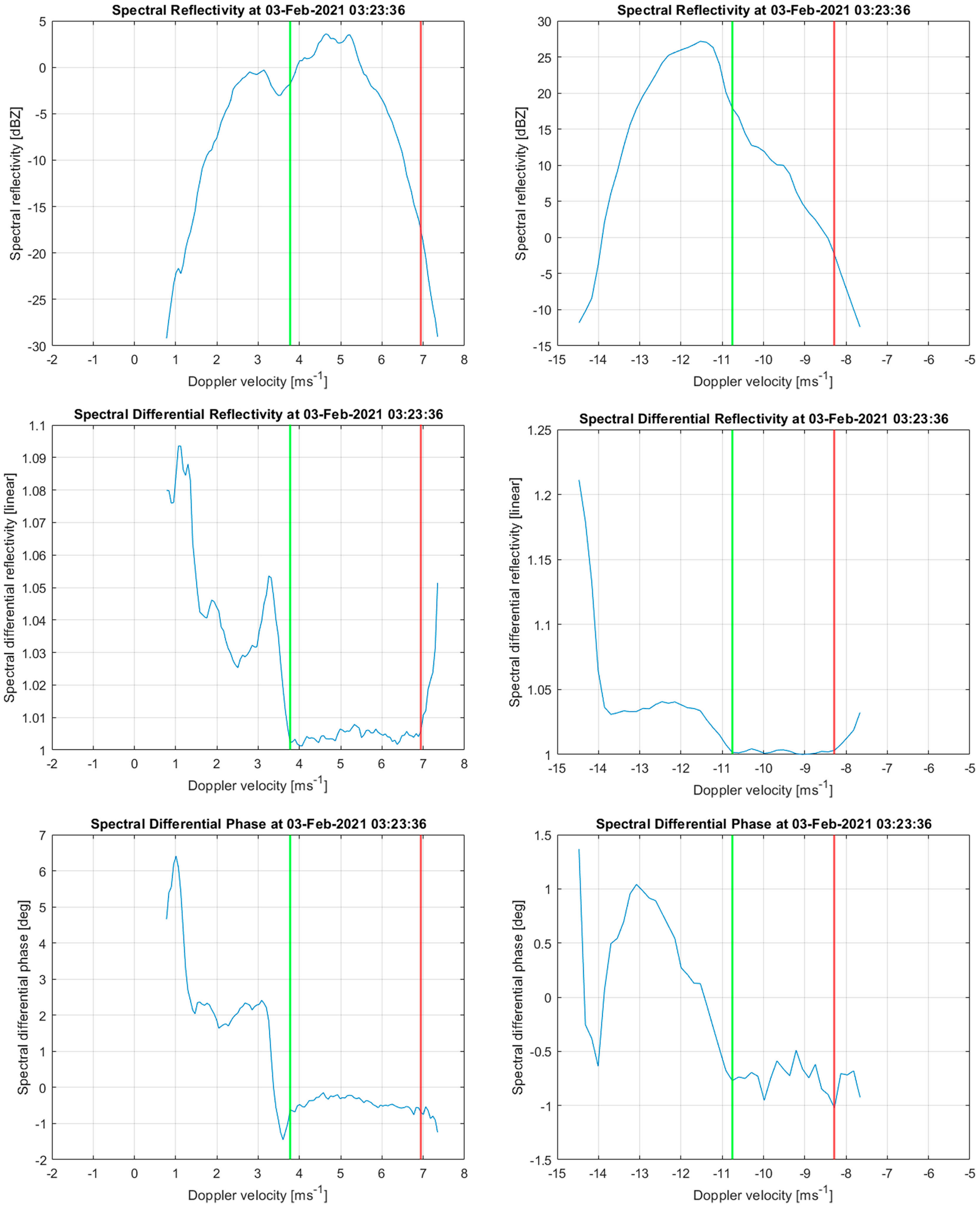

FIG. 11. Examples of Rayleigh plateau detection at both frequencies, (left) 94 GHz and (right) 35 GHz in the Doppler spectra at a specific height (253 m) and time. The red and green lines represent the right (smallest raindrops) and left (largest raindrops) Rayleigh plateau boundaries, respectively.

the scattering of raindrops can still be described by Rayleigh scattering.

b. Confidence interval

The estimation of the experimental uncertainty associated with the differential backscatter phase can be achieved by considering the uncertainty estimates of both the differential propagation phase and the differential phase. As an initial approximation, it is anticipated that the uncertainty of the differential phase will be smaller than that of the differential propagation phase due to the utilization of a retrieval technique and a limited number of Doppler bins. Consequently, the uncertainty of the differential propagation phase can serve as an approximation of the experimental uncertainty pertaining to the differential backscatter phase. The influence of the polarimetric calibration error on the differential phase is disregarded as it does not impact the

TABLE 2. Rayleigh plateau detection of the profile at 0323:36 UTC 3 Feb 2021 [selected heights, Rayleigh Doppler width, Rayleigh plateau spectral differential reflectivity, and differential propagation phase (mean and standard deviation)]. The top value and the bottom value (in italics) relate to 35 and 94 GHz, respectively.

Height (m)	105.4	210.8	295.2	400.6	506.0	590.3	716.8	801.2
Doppler width (m s^{-1})	2.78	2.62	2.31	1.54	2.31	1.85	2.31	2.47
	3.62	*3.44*	*3.50*	*3.21*	*3.04*	*2.98*	*2.53*	*2.30*
Mean sz_{dr} (linear)	1.008	1.006	1.005	0.995	0.994	0.991	0.987	0.982
	1.009	*1.004*	*1.007*	*1.001*	*1.000*	*0.998*	*0.997*	*0.995*
Std sz_{dr} (linear)	0.0020	0.0025	0.0015	0.0019	0.0024	0.0029	0.0037	0.0026
	0.0025	*0.0015*	*0.0019*	*0.0021*	*0.0025*	*0.0025*	*0.0025*	*0.0024*
Mean $s\Phi_{dp}$ (°)	−0.74	−0.80	−0.76	−0.56	−0.40	−0.30	−0.47	−0.47
	−0.16	*−0.38*	*−0.49*	*−0.66*	*−0.80*	*−0.90*	*−0.96*	*−0.96*
Std $s\Phi_{dp}$ (°)	0.08	0.09	0.11	0.10	0.12	0.08	0.15	0.20
	0.15	*0.16*	*0.18*	*0.20*	*0.21*	*0.18*	*0.15*	*0.17*

estimation of δ_{co}. Considering the limited data available in the Rayleigh plateau, the bootstrapping resampling method is employed to obtain the 95% confidence interval for the experimental differential backscatter phase ($\Delta\delta_{co}^{exp}$).

Additionally, a fixed uncertainty of ±0.15°, accounting for the effects of various shape–size relationships, is incorporated ($\Delta\delta_{co}^{mod}$). Figure 13 demonstrates the significant influence of different shape–size relationships on the values of the differential backscatter phase. In this study, the KAB (middle mode), described in section 2, is employed as the chosen shape–size relationship.

c. *Time series of δ_{co}*

Figure 14 presents a time series depicting the retrieved differential backscatter phase. The series confirms the expected order of magnitude for δ_{co} values at 35 and 94 GHz. Specifically, the differential backscatter phase tends to be higher at 35 GHz compared to 94 GHz, for both the simulation and the retrieval. However, for small mass-weighted mean diameters below 0.5 mm, the trend is reversed, with larger δ_{co} values observed at 94 GHz. This indicates a greater sensitivity to the characterization of smaller raindrops at this frequency.

6. Estimation of the mass-weighted mean diameter

By ensuring consistency in the time and height of the estimated differential backscatter phase at 35 and 94 GHz, the retrieval of the mass-weighted mean diameter D_m, one of the parameters of the gamma-modeled raindrop size distribution, becomes feasible. To derive D_m from δ_{co}, we introduce a

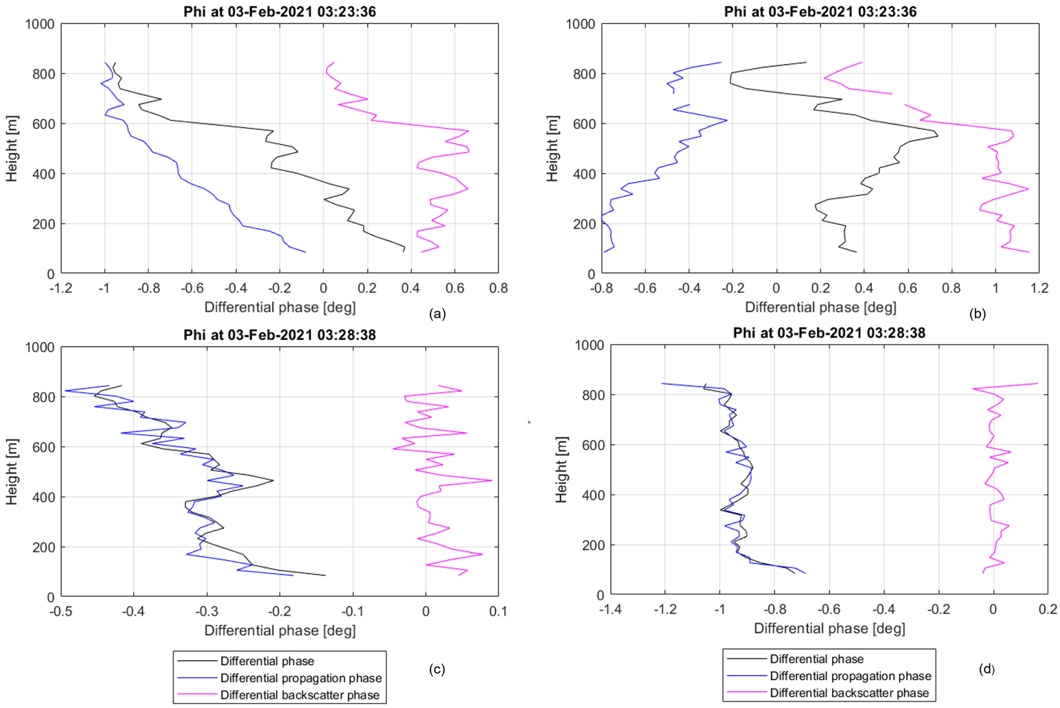

FIG. 12. Examples of profiles of the measured differential phase and the obtained differential propagation phase and differential backscatter phase. (left) 94 GHz. (right) 35 GHz. The rainfall rate: (top) 15 and (bottom) 1 mm h^{-1}.

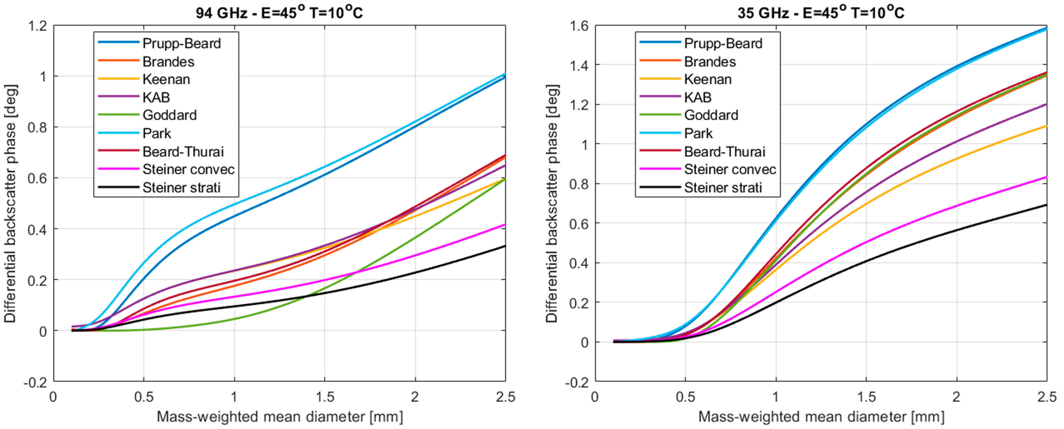

FIG. 13. Simulated differential backscatter phase versus mass-weighted mean diameter using different shape–size relationships. A canting angle distribution with a standard deviation of 7° is included for the wobbling of raindrops (Mardia axial distribution, $\kappa = 30$).

second automated algorithm that leverages simulation outcomes (see Fig. 15). The simulation is the same as described in section 2. The D_m values are posited within the range of 0.1–2.5 mm, with the shape parameter μ varying from -2 to 8. The simulation employs a resolution of 0.01 mm for D_m and 0.1 for μ. It should be noted that larger values of μ could be obtained when considering narrow raindrop size distributions measured by disdrometers due to their smaller sampling area. As depicted in Fig. 2, there is a significant sensitivity of δ_{co} to D_m, whereas the sensitivity to μ is relatively minor. The aforementioned trait renders δ_{co} a primary estimator for D_m.

In practical applications, a confidence interval for δ_{co} values is obtained at each height and time for both frequency bands. Utilizing the simulations from Fig. 15, this interval could result in a two-dimensional confidence interval for D_m and μ. However, due to the relatively large confidence interval of δ_{co} and limited sensitivity to μ, the focus is primarily directed toward retrieving D_m alone, with the aim of reducing its confidence interval through the combined use of radar frequencies.

It should be noted that the estimation of the mass-weighted mean diameter is not performed under certain conditions, such as when the rainfall rate recorded by the weather station is 0 mm h^{-1}, the Rayleigh plateau detection is not achieved, or when the differential backscatter phase is negative.

Let us illustrate the estimation procedure. Initially, we restrict our focus to the 95% confidence interval for δ_{co}, neglecting the potential influence of a shape–size relationship markedly different from KAB. The delineated δ_{co} interval yields a 2D range in D_m and μ. The resultant 2D intervals are presented in the first and second columns of Fig. 16, corresponding to frequencies of 94 and 35 GHz, respectively. The three rows correspond to different times (1200, 1230, and 1300 UTC) in the study case (refer to Fig. 14 for the corresponding values of δ_{co}). At a fixed frequency, a well-determined D_m interval is evident; however, the μ interval is generally

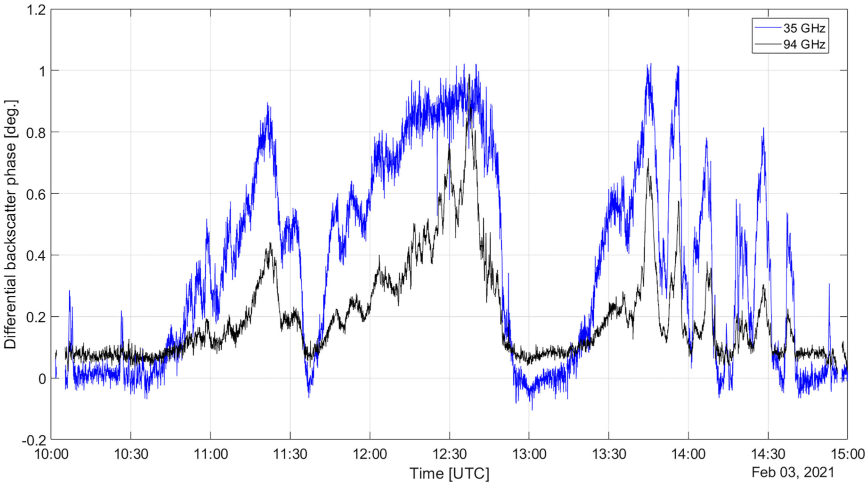

FIG. 14. Time series of the averaged differential backscatter phase at low heights (169–211 m).

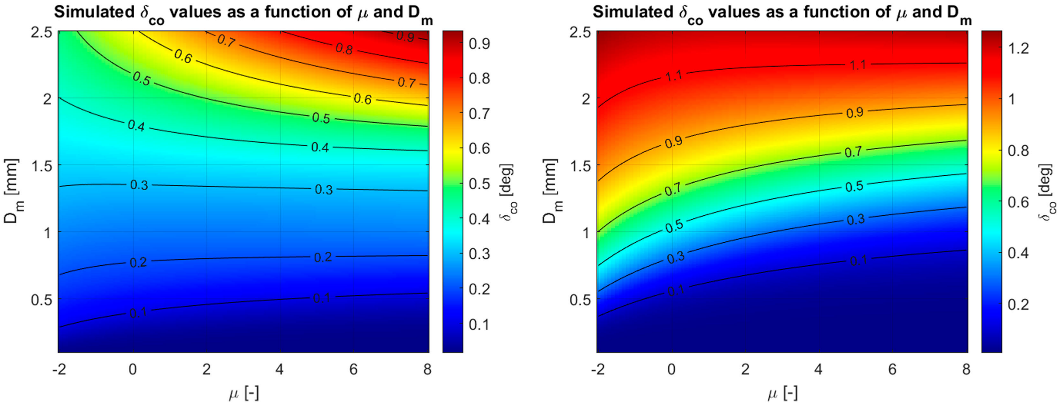

FIG. 15. Simulated differential backscatter phase versus mass-weighted mean diameter and shape parameter at the frequencies (left) 94 and (right) 35 GHz. The KAB shape–size relationship and Mardia axial distribution with $\kappa = 30$ is used.

broader, spanning the complete range $[-2, 8]$. Combining the 2D intervals for both frequencies and determining their intersection (third column) typically yields a more precise 2D interval $[D_m, \mu]$. Yet, in instances where large D_m values are expected in the study case, no intersection between the 2D intervals (94 and 35 GHz) occurs, as exemplified in the third column of row 2 (Fig. 16). Consequently, an alternative output is generated (fourth column), wherein the input interval for δ_{co} is extended to $[\delta_{\text{co}} - \Delta\delta_{\text{co}}^{\text{exp}} - \Delta\delta_{\text{co}}^{\text{mod}}, \delta_{\text{co}} + \Delta\delta_{\text{co}}^{\text{exp}} + \Delta\delta_{\text{co}}^{\text{mod}}]$, ensuring consistent intersections. While the resultant mean D_m value undergoes slight adjustment, the precision in D_m is diminished. In most cases, obtaining a μ interval smaller than $[-2, 8]$ proves impractical.

These 2D intervals yield a minimum (D_m^{min}), maximum (D_m^{max}), and mean value (D_m^{mean}) for the mass-weighted mean diameter. A representative time series is depicted in Fig. 17. When considering only the experimental error of δ_{co}, the dual-frequency retrieval of D_m exhibits high precision; however,

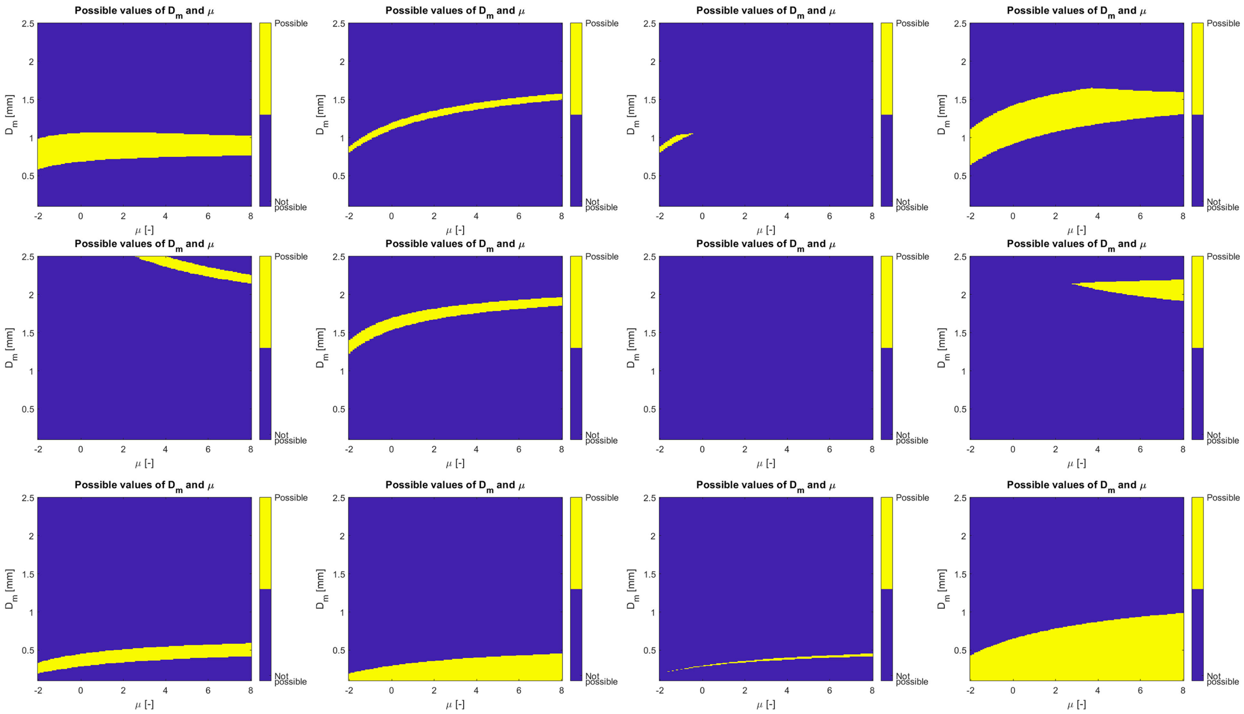

FIG. 16. D_m–μ 2D intervals obtained from differential backscatter phase retrieval. The columns represent the results obtained at (first column) 94 GHz, (second column) 35 GHz, (third column) combined 94 and 35 GHz, and (fourth column) combined 94 and 35 GHz with the extension of the error on δ_{co} with $\Delta\delta_{\text{co}}^{\text{mod}}$. The rows correspond to different times: (top) 1200 UTC (2.9 mm h^{-1}), (middle) 1230 UTC (4.6 mm h^{-1}), and (bottom) 1300 (0.6 mm h^{-1}).

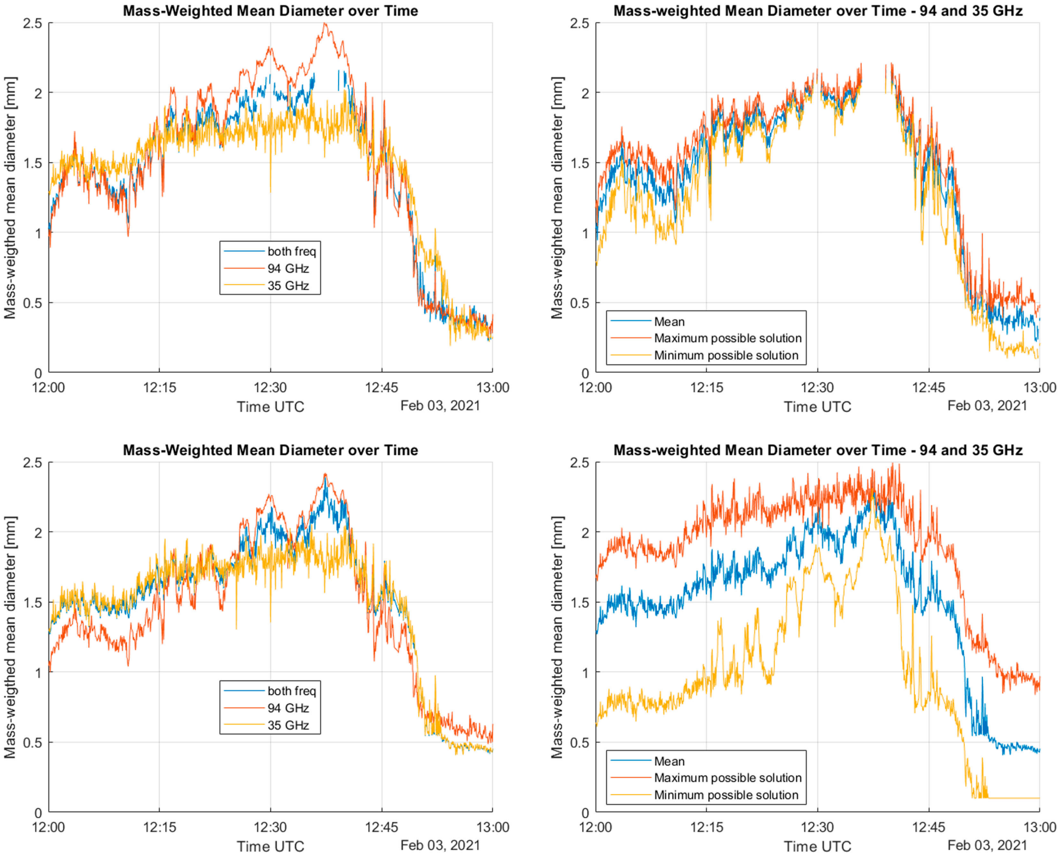

FIG. 17. Mass-weighted mean diameter versus time at low heights (169–211 m). (left) The time series of D_m^{mean} at low heights. (right) The dual-frequency D_m^{min} (orange), D_m^{mean} (blue), and D_m^{max} (red) are plotted. What differs between the two rows is the (top) absence or (bottom) addition of $\Delta\delta_{\mathrm{co}}^{\mathrm{mod}}$ as input for D_m estimation.

certain peak values are absent (second column, first row). Introducing a modeling error by augmenting the error of δ_{co} leads to the retrieval of these peak values, yet the precision diminishes for smaller values of dual-frequency D_m (second column, second row). At this juncture, it becomes crucial to juxtapose the mass-weighted mean diameter retrievals with in situ measurements. To fulfill this objective, the measurements from a nearby disdrometer are taken into account.

7. A first comparison with disdrometer data

The estimation of the mass-weighted mean diameter using simulations and differential backscatter phase estimation will be compared with D_m directly obtained from the raindrop size distribution measured by the disdrometer located at ground level. Since the cloud radar does not observe rainfall at ground level, only height bins at relatively low altitudes will be considered for the comparison. Specifically, the average of the fifth–seventh height bins, spanning the range of 169–211 m, will be used to minimize the impact of random errors. It is assumed that the raindrop size distribution remains constant within this height range. In this work, the correction for evaporation proposed in Myagkov et al. (2020) was not investigated.

A time lag correction of 2 min is applied to the D_m time series. This adjustment is made because the D_m peaks retrieved from the cloud radar slightly preceded the D_m peaks from the disdrometer. The time lag correction is determined by identifying the time lag exhibiting the maximum cross correlation between D_m retrieved by the cloud radar and D_m calculated from the disdrometer RDSD. Prior to this correction, the time resolution of the retrieved D_m is reduced to 1 min to match the time resolution of the calculated D_m. The time lag between the mass-weighted mean raindrop diameter time series likely arises from the 150-m distance between the two sensors. The cloud radar is situated west of the disdrometer and profiles in a slantwise manner toward the west, where the horizontal wind originates. Additionally, the disdrometer has a time resolution of 1 min, while the cloud radar has a time resolution of 3.6 s. These factors contribute to the earlier peaks of D_m observed in the cloud radar data.

Figures 18 and 19 illustrate the comparison between the cloud radar's D_m retrieval and the disdrometer's D_m. Overall, there is a strong correlation between the maxima and minima of the mass-weighted mean raindrop diameters, indicating the capability of the cloud radar to capture small-scale rainfall variability. For D_m values below 1 mm as recorded by the disdrometer, the cloud radar's D_m values are consistently smaller

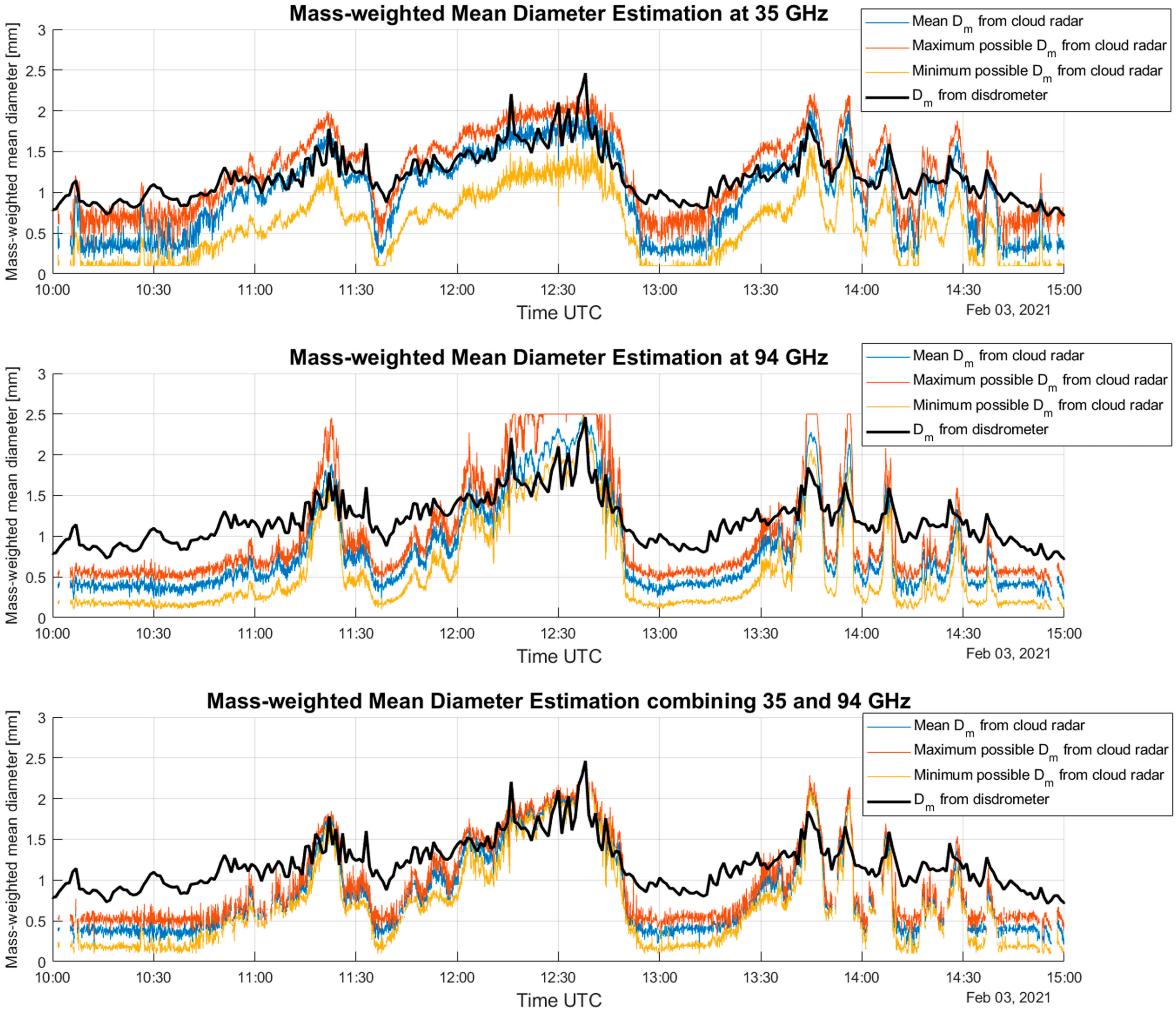

FIG. 18. Comparison of the cloud radar and Parsivel disdrometer mass-weighted mean diameter. The cloud radar D_m interval relates to the experimental error on δ_{co}.

than those of the disdrometer. This discrepancy may arise from potential overestimation in the disdrometer's D_m, owing to limitations in Parsivel disdrometer's measurement capabilities for small raindrops below 0.375 mm. However, overall agreement with the mean D_m retrieved by the cloud radar is observed. The utilization of both frequencies for D_m estimation serves to narrow the confidence interval of the mass-weighted mean diameter.

Comparison of results between Figs. 18 and 19, in terms of cloud radar mean D_m, reveals similarity, aligning with expectations, as the expansion of the error interval of δ_{co} should minimally impact the mean D_m. Generally, there is an overlap in the 2D interval of D_m–μ at 35 and 94 GHz when considering only the experimental error on δ_{co} (Fig. 18; bottom). However, exceptions arise, such as at 1237 UTC for the D_m peak value of 2.5 mm and occasionally for low D_m values. A reliable estimation of the peak value is achieved at 94 GHz, with overlapping between 35 and 94 GHz facilitated by augmenting the 95% confidence interval of δ_{co} with a model error. Figure 14 illustrates that, for this 2.5-mm peak value, the estimated differential backscatter phase is approximately 1° at both 35 and 94 GHz. None of the shape–size relationships considered in Fig. 13 can account for this discrepancy. Regarding the overlapping of 2D D_m–μ intervals, the scenario aligns with the second row of Fig. 16, where the mean value of μ is relatively high for a gamma distribution with a large D_m, suggesting that the gamma distribution model for the raindrop size distribution may not be applicable during this specific time.

In evaluating the appropriate outcome for describing D_m at this juncture, consideration must be given to the choice of frequency or error interval for the differential backscatter phase, as depicted in Fig. 20. This figure presents various D_m scatterplots, each differing in the selection of frequency or error interval. Notably, when the error interval of δ_{co} is increased, an

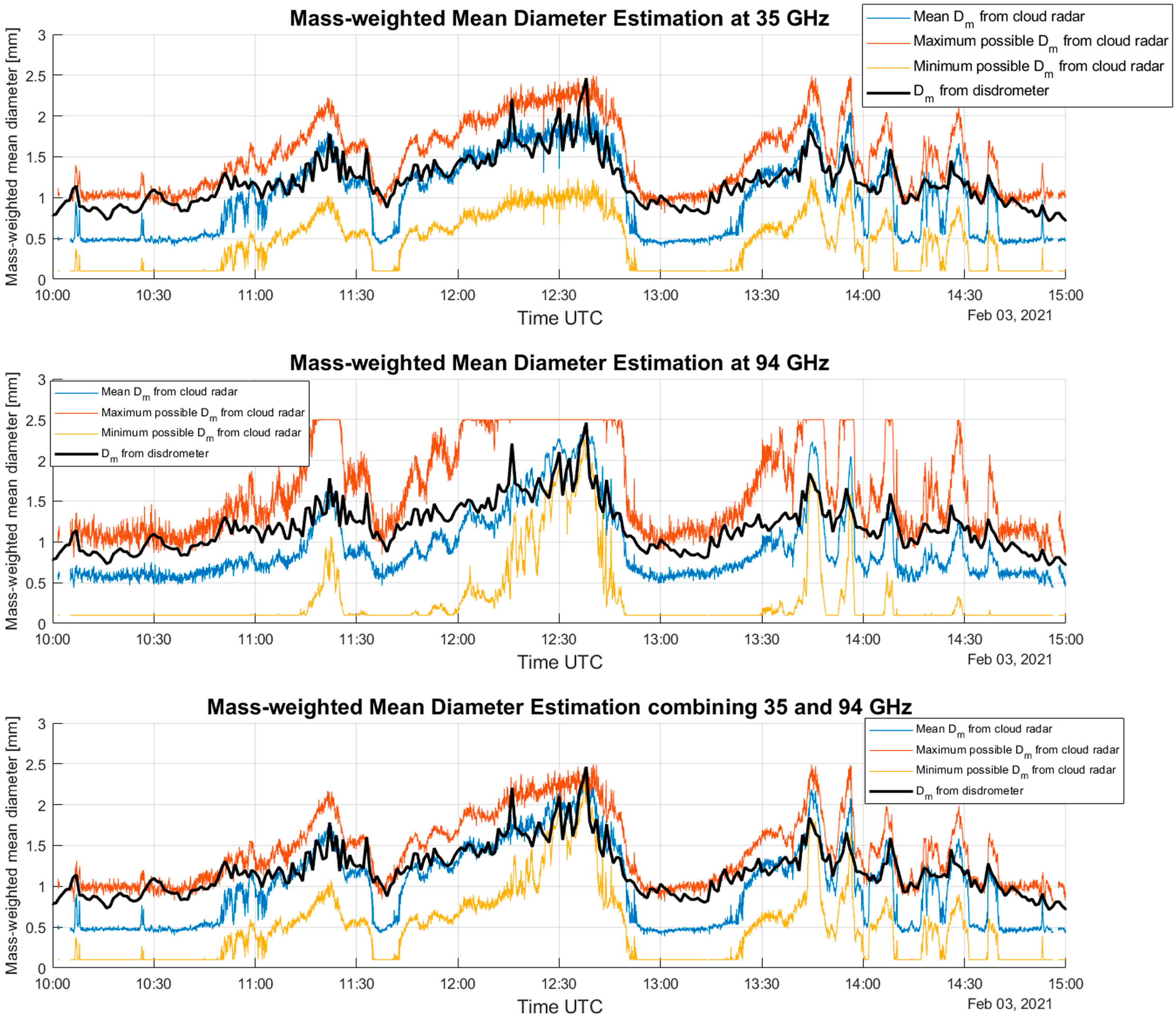

FIG. 19. Comparison of the cloud radar and Parsivel disdrometer mass-weighted mean diameter. The cloud radar D_m interval relates to the experimental and modeling errors on δ_{co}.

enhancement in estimating small D_m values is observed. From this observation, we may conclude that the cloud radar's D_m below 1 mm may be underestimated, with a corresponding overestimation in the disdrometer's D_m. For the cloud radar retrieval, this discrepancy may be attributed to the shape–size relationship chosen for small raindrops. A more accurate estimation of D_m corresponding to the second row of Fig. 20 is achieved by utilizing the input $\delta_{\mathrm{co}} \pm (\Delta\delta_{\mathrm{co}}^{\mathrm{exp}} + \Delta\delta_{\mathrm{co}}^{\mathrm{mod}})$. Introducing a model error allows for potential deviations in terms of the shape–size relationship or gamma model. For stratiform rain, Gatidis et al. (2020) demonstrated that the raindrop size distribution is typically not strictly gamma but is close to the gamma model. It is noteworthy that the D_m retrieval at 94 GHz may experience slight underestimation up to 1.5 mm, while the one at 35 GHz may be underestimated below 1 mm and from 2 mm onward. The optimal result is obtained through the combination of 35 and 94 GHz (second row, third column), not solely based on the statistics of Δ (the difference between disdrometer's D_m and cloud radar's D_m) but also on the agreement from 1 mm and the reduction in the confidence interval of D_m.

For comprehensive understanding, it is essential to acknowledge the significant impact of the raindrop canting angle distribution on this second retrieval technique (D_m estimation). Canting reduces the value of the differential backscatter phase, as detailed in section 2a. Initial results, excluding the contribution of canting, showed D_m underestimation across the entire range. In such instances, using the input $\delta_{\mathrm{co}} \pm \Delta\delta_{\mathrm{co}}^{\mathrm{exp}}$, there were frequent occurrences of nonoverlapping (more than 50%) 2D intervals D_m–μ combining 35 and 94 GHz.

8. Conclusions

The objective of this research is to investigate radar polarimetry and spectral polarimetry at high frequencies

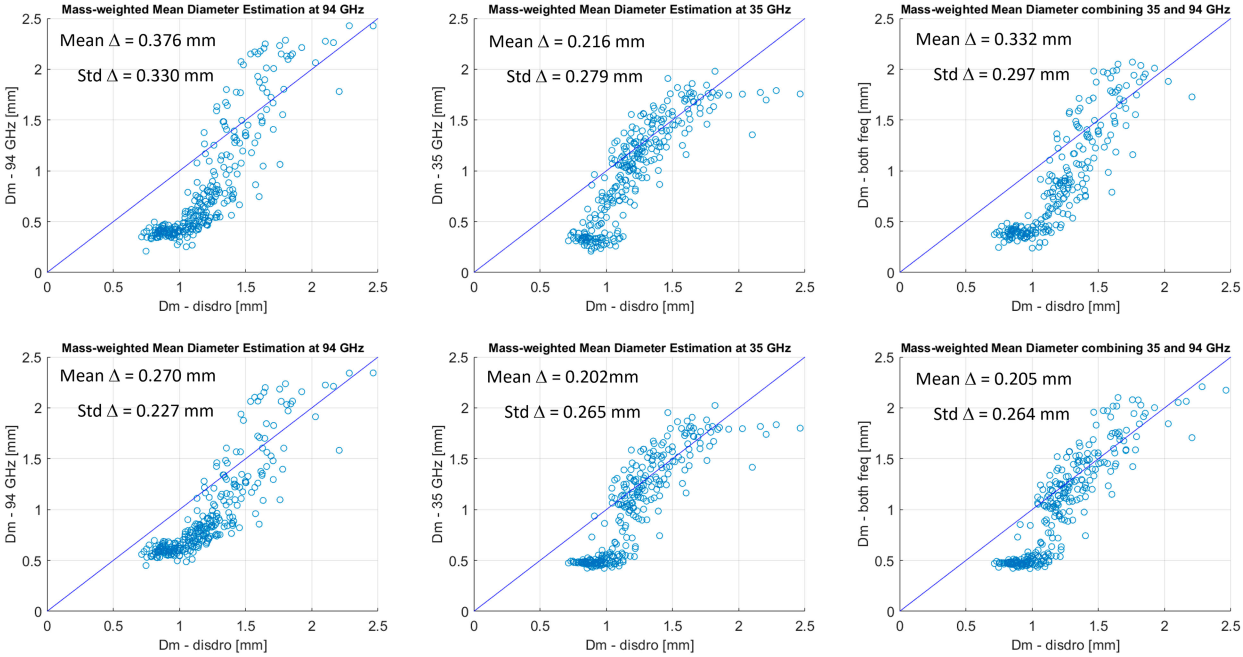

FIG. 20 Scatterplots of the mass-weighted mean diameter. The input for the D_m retrieval is (top) $\delta_{\mathrm{co}} \pm \Delta\delta_{\mathrm{co}}^{\mathrm{exp}}$ and (bottom) $\delta_{\mathrm{co}} \pm (\Delta\delta_{\mathrm{co}}^{\mathrm{exp}} + \Delta\delta_{\mathrm{co}}^{\mathrm{mod}})$. The statistics of the difference Δ between disdrometer's D_m and cloud radar's D_m, are given in terms of mean and standard deviation.

(millimeter-wavelength) in order to retrieve rain microphysics. The aim is to acquire vertical or slant profiles of raindrop size distribution (RDSD) with high spatial and temporal resolution, enabling the understanding of small-scale rain processes. However, the presence of attenuation, which increases with rainfall rate and frequency, restricts this investigation to light and moderate rain. In the case of weather radars (centimeter-wavelength), a valuable polarimetric radar variable for estimating mean raindrop diameter is differential reflectivity Z_{dr}. However, for cloud radars (millimeter-wavelength), especially at 94 GHz, Z_{dr} exhibits minimal values due to the integration of Mie oscillations, rendering it insensitive to changes in the raindrop size distribution. Consequently, the differential backscatter phase δ_{co} replaces this variable. Since δ_{co} is derived from the differential phase and is not affected by attenuation or polarimetric calibration, it is a preferred choice at high frequencies for retrieving raindrop mean diameter.

The challenge lies in separating the differential propagation phase Φ_{dp} from δ_{co}. This can be achieved by analyzing the Doppler spectra of the measured differential phase Ψ_{dp}. This article proposes an automatic technique that disentangles the differential backscatter phase without requiring Doppler dealiasing. The technique is based on two spectral polarimetric radar variables, namely, spectral differential reflectivity sZ_{dr} and spectral differential phase $s\Psi_{\mathrm{dp}}$. These variables clearly indicate the Doppler velocities at which small raindrops, associated with Rayleigh scattering, are present. Within this Rayleigh Doppler velocity interval, the spectral differential phase corresponds to the differential propagation phase. Subsequently, δ_{co} is obtained by subtracting the estimated Φ_{dp} from the measured Ψ_{dp}. Using this methodology, profiles of differential backscatter phase, differential propagation phase, and subsequently K_{dp} and specific differential attenuation can be obtained. The focus of the paper primarily centers around the differential backscatter phase.

In the case study time series, where rainfall rates range from 0 to 7.5 mm h^{-1}, δ_{co} exhibits values between 0° and 1°, with higher values observed at 35 GHz compared to 94 GHz, as predicted by simulations. The experimental 95% confidence interval of δ_{co} is obtained using the resampling method known as bootstrapping. Additionally, an error associated with the choice of axis ratio–size model is introduced.

In our analysis, simulations incorporating the differential backscatter phase with confidence interval against the mass-weighted mean diameter D_m and shape parameter μ of the gamma-modeled raindrop size distribution are employed to estimate D_m at both 35 and 94 GHz frequencies. Utilizing another automatic method outputs 2D interval D_m–μ through these simulations. When employing a single frequency, it is possible to retrieve the corresponding D_m confidence interval, but there is typically minimal or no reduction in the input interval of μ. However, the integration of both frequencies, 35 and 94 GHz, yields improved results by decreasing confidence intervals. In summary, D_m with its associated confidence interval is successfully retrieved, whereas the same is generally not achievable for the shape parameter due to its excessively large confidence interval.

The D_m values retrieved at both cloud radar frequencies are subsequently compared to the mass-weighted mean diameter directly calculated from collocated disdrometer data. The robust correlation observed between these diameters underscores the cloud radar's potential in capturing small-scale variations in rain microphysics. Overall, a commendable agreement is noted between the cloud radar's D_m and the disdrometer's D_m for D_m values greater than 1 mm. However, for lower D_m values, a combination of factors may contribute to the observed discrepancies. The mass-weighted mean diameter derived from disdrometer data tends to be overestimated, while the cloud radar retrieval is likely underestimated in this light rain regime. This underestimation could stem from the chosen shape–size relationship in the simulation.

Considering the entire spectrum of D_m values, the mean difference between the disdrometer's D_m and cloud radar's D_m is 0.2 mm. Based on this initial comparison, preference is given to the D_m retrieval based on the combination of 35 and 94 GHz, incorporating a model error in the differential backscatter phase to accommodate potential deviations in the shape–size relationship and/or gamma model of the raindrop size distribution. Nonetheless, the results from single-frequency retrievals are also noteworthy, albeit with larger confidence intervals.

In light of these preliminary findings, with a particular emphasis on the potential for estimating the mean raindrop diameter using the differential backscatter phase, which is unaffected by attenuation and polarimetric calibration, it is evident that further research should be conducted using other polarimetric and spectral polarimetric radar variables at high frequencies to retrieve the raindrop size distribution with high spatial and temporal resolution.

Acknowledgments. The authors thank (Rob Mackenzie, Mahaut Sourzac) and (Saverio Guzzo, André Castro) for their support for maintaining the cloud radar and disdrometer operational and for data management, respectively. Further, Christos Gatidis provided a time series of D_m using the methodology described in Gatidis et al. (2020) for the first comparison of cloud radar retrieved mass-weighted mean diameter. This work used instruments and data of the Ruisdael Observatory, a scientific research infrastructure cofinanced by the Netherlands Organization for Scientific Research (NWO), Grant 184.034.015.

Data availability statement. The data used in this article are available upon request.

REFERENCES

Andsager, K., K. V. Beard, and N. F. Laird, 1999: Laboratory measurements of axis ratios for large raindrops. *J. Atmos. Sci.*, **56**, 2673–2683, https://doi.org/10.1175/1520-0469(1999)056<2673:LMOARF>2.0.CO;2.

Atlas, D., R. C. Srivastava, and R. S. Sekhon, 1973: Doppler radar characteristics of precipitation at vertical incidence. *Rev. Geophys.*, **11**, 1–35, https://doi.org/10.1029/RG011i001p00001.

Aydin, K., and Y.-M. Lure, 1991: Millimeter wave scattering and propagation in rain: A computational study at 94 and 140 GHz for oblate spheroidal and spherical raindrops. *IEEE Trans. Geosci. Remote Sens.*, **29**, 593–601, https://doi.org/10.1109/36.135821.

Beard, K. V., and C. Chuang, 1987: A new model for the equilibrium shape of raindrops. *J. Atmos. Sci.*, **44**, 1509–1524, https://doi.org/10.1175/1520-0469(1987)044<1509:ANMFTE>2.0.CO;2.

Bringi, V. N., and V. Chandrasekar, 2001: *Polarimetric Doppler Weather Radar: Principles and Applications*. Cambridge University Press, 636 pp.

Bühl, J., R. Leinweber, U. Görsdorf, M. Radenz, A. Ansmann, and V. Lehmann, 2015: Combined vertical-velocity observations with Doppler lidar, cloud radar and wind profiler. *Atmos. Meas. Tech.*, **8**, 3527–3536, https://doi.org/10.5194/amt-8-3527-2015.

Gatidis, C., M. Schleiss, C. Unal, and H. Russchenberg, 2020: A critical evaluation of the adequacy of the gamma model for representing raindrop size distributions. *J. Atmos. Oceanic Technol.*, **37**, 1765–1779, https://doi.org/10.1175/JTECH-D-19-0106.1.

——, ——, and ——, 2022: Sensitivity analysis of DSD retrievals from polarimetric radar in stratiform rain based on the μ-Λ relationship. *Atmos. Meas. Tech.*, **15**, 4951–4969, https://doi.org/10.5194/amt-15-4951-2022.

Hogan, R. J., N. Gaussiat, and A. J. Illingworth, 2005: Stratocumulus liquid water content from dual-wavelength radar. *J. Atmos. Oceanic Technol.*, **22**, 1207–1218, https://doi.org/10.1175/JTECH1768.1.

Holt, A., N. Uzunoglu, and B. Evans, 1978: An integral equation solution to the scattering of electromagnetic radiation by dielectric spheroids and ellipsoids. *IEEE Trans. Antennas Propag.*, **26**, 706–712, https://doi.org/10.1109/TAP.1978.1141916.

Illingworth, A. J., and Coauthors, 2007: Cloudnet. *Bull. Amer. Meteor. Soc.*, **88**, 883–898, https://doi.org/10.1175/BAMS-88-6-883.

Jameson, A. R., and A. B. Kostinski, 2001: What is a raindrop size distribution? *Bull. Amer. Meteor. Soc.*, **82**, 1169–1178, https://doi.org/10.1175/1520-0477(2001)082<1169:WIARSD>2.3.CO;2.

Keenan, T. D., L. D. Carey, D. S. Zrnić, and P. T. May, 2001: Sensitivity of 5-cm wavelength polarimetric radar variables to raindrop axial ratio and drop size distribution. *J. Appl. Meteor.*, **40**, 526–545, https://doi.org/10.1175/1520-0450(2001)040<0526:SOCWPR>2.0.CO;2.

Kneifel, S., A. von Lerber, J. Tiira, D. Moisseev, P. Kollias, and J. Leinonen, 2015: Observed relations between snowfall microphysics and triple-frequency radar measurements. *J. Geophys. Res. Atmos.*, **120**, 6034–6055, https://doi.org/10.1002/2015JD023156.

Kollias, P., B. A. Albrecht, and F. Marks Jr., 2002: Why Mie? *Bull. Amer. Meteor. Soc.*, **83**, 1471–1484, https://doi.org/10.1175/BAMS-83-10-1471.

——, E. E. Clothiaux, M. A. Miller, B. A. Albrecht, G. L. Stephens, and T. P. Ackerman, 2007: Mm-wavelength radars: New frontier in atmospheric cloud and precipitation research. *Bull. Amer. Meteor. Soc.*, **88**, 1608–1624, https://doi.org/10.1175/BAMS-88-10-1608.

——, and Coauthors, 2020: The ARM radar network: At the leading edge of cloud and precipitation observations. *Bull. Amer. Meteor. Soc.*, **101**, E588–E607, https://doi.org/10.1175/BAMS-D-18-0288.1.

Küchler, N., S. Kneifel, U. Löhnert, P. Kollias, H. Czekala, and T. Rose, 2017: A W-band radar–radiometer system for accurate and continuous monitoring of clouds and precipitation. *J. Atmos. Oceanic Technol.*, **34**, 2375–2392, https://doi.org/10.1175/JTECH-D-17-0019.1.

Kumjian, M. R., and A. V. Ryzhkov, 2012: The impact of size sorting on the polarimetric radar variables. *J. Atmos. Sci.*, **69**, 2042–2060, https://doi.org/10.1175/JAS-D-11-0125.1.

Liebe, H. J., G. A. Hufford, and T. Manabe, 1991: A model for the complex permittivity of water at frequencies below 1 THz. *Int. J. Infrared Millimeter Waves*, **12**, 659–675, https://doi.org/10.1007/BF01008897.

Mardia, K. V., 1972: *Statistics of Directional Data*. Academic Press, 357 pp.

Mason, S. L., J. C. Chiu, R. J. Hogan, and L. Tian, 2017: Improved rain rate and drop size retrievals from airborne Doppler radar. *Atmos. Meas. Tech.*, **17**, 11 567–11 589, https://doi.org/10.5194/acp-17-11567-2017.

Matrosov, S. Y., 2017: Characteristic raindrop size retrievals from measurements of differences in vertical Doppler velocities at Ka- and W-band radar frequencies. *J. Atmos. Oceanic Technol.*, **34**, 65–71, https://doi.org/10.1175/JTECH-D-16-0181.1.

Moisseev, D. N., and V. Chandrasekar, 2007: Nonparametric estimation of the raindrop size distribution from dual-polarization radar spectral observations. *J. Atmos. Oceanic Technol.*, **24**, 1008–1018, https://doi.org/10.1175/JTECH2024.1.

Mugnai, A., and Coauthors, 2005: Snowfall measurements by the proposed European GPM mission. *Measuring Precipitation from Space: EURAINSAT and the Future*, V. Levizzani, P. Bauer, and J. F. Turk, Eds., Springer, 655–674.

Myagkov, A., S. Kneifel, and T. Rose, 2020: Evaluation of the reflectivity calibration of W-band radars based on observations in rain. *Atmos. Meas. Tech.*, **13**, 5799–5825, https://doi.org/10.5194/amt-13-5799-2020.

Otto, T., and H. W. J. Russchenberg, 2011: Estimation of specific differential phase and differential backscatter phase from polarimetric weather radar measurements of rain. *IEEE Geosci. Remote Sens. Lett.*, **8**, 988–992, https://doi.org/10.1109/LGRS.2011.2145354.

Overeem, A., E. van den Besselaar, G. van der Schrier, J. Fokke Meirink, E. van der Plas, and H. Leijnse, 2023: EURADCLIM: The European climatological high-resolution gauge-adjusted radar precipitation dataset. *Earth Syst. Sci. Data*, **15**, 1441–1464, https://doi.org/10.5194/essd-15-1441-2023.

Peters, G., B. Fischer, H. Münster, M. Clemens, and A. Wagner, 2005: Profiles of raindrop size distributions as retrieved by microrain radars. *J. Appl. Meteor.*, **44**, 1930–1949, https://doi.org/10.1175/JAM2316.1.

Thurai, M., C. R. Williams, and V. N. Bringi, 2014: Examining the correlations between drop size distribution parameters using data from two side-by-side 2D-video disdrometers. *Atmos. Res.*, **144**, 95–110, https://doi.org/10.1016/j.atmosres.2014.01.002.

Tridon, F., and A. Battaglia, 2015: Dual-frequency radar Doppler spectral retrieval of raindrop size distributions and entangled dynamics variables. *J. Geophys. Res. Atmos.*, **120**, 5585–5601, https://doi.org/10.1002/2014JD023023.

——, ——, E. Luke, and P. Kollias, 2017: Rain retrieval from dual-frequency radar Doppler spectra: Validation and potential for a midlatitude precipitating case-study. *Quart. J. Roy. Meteor. Soc.*, **143**, 1364–1380, https://doi.org/10.1002/qj.3010.

Unal, C., 2015: High-resolution raindrop size distribution retrieval based on the Doppler spectrum in the case of slant profiling radar. *J. Atmos. Oceanic Technol.*, **32**, 1191–1208, https://doi.org/10.1175/JTECH-D-13-00225.1.

Williams, C. R., 2002: Simultaneous ambient air motion and raindrop size distributions retrieved from UHF vertical incident profiler observations. *Radio Sci.*, **37**, 1024, https://doi.org/10.1029/2000RS002603.

Yu, T.-Y., X. Xiao, and Y. Wang, 2012: Statistical quality of spectral polarimetric variables for weather radar. *J. Atmos. Oceanic Technol.*, **29**, 1221–1235, https://doi.org/10.1175/JTECH-D-11-00090.1.